



Full length article

Modeling competitive adsorption and diffusion of CH₄/CO₂ mixtures confined in mature type-II kerogen: Insights from molecular dynamics simulations

Patrick A. Bonnaud, Fouad Oulebsir, Guillaume Galliero, Romain Vermorel *

Université de Pau et des Pays de L'Adour, E2S UPPA, CNRS, TotalEnergies, LFCR, Pau, France

ARTICLE INFO

Keywords:

Kerogen
Molecular dynamics
Adsorption
Diffusion
Selectivity
Mixture separation
Carbon dioxide
Methane

ABSTRACT

In this study, the adsorption and competitive diffusion of methane (CH₄) and carbon dioxide (CO₂) mixtures through a molecular model of mature type-2 kerogen was investigated using molecular dynamics simulations. The Dual Control Volume-Grand Canonical Molecular Dynamics method was used to analyze the system and the results were focused on the selectivity of kerogen towards mixtures under a wide range of thermodynamic conditions. The results showed that the adsorption selectivity of CO₂/CH₄ was around 2–4 and decreased with temperature in the range 350–450 K. The Extended Langmuir (EL) model was found to underestimate the selectivity, and a correction was proposed in the form of the Corrected Extended Langmuir (CEL) model, which improved the estimations of the adsorption of CH₄/CO₂ mixtures in kerogen with only one adjustable parameter independent of thermodynamic conditions. Interestingly, we noticed that, out of equilibrium, the adsorption selectivity was not affected by the flow conditions when a pressure gradient was imposed, and the CEL model can thus be used to describe the contribution of adsorption to the selectivity under flow conditions. The results showed that the ratio of the collective diffusion coefficients of CH₄ and CO₂ was around 0.3–0.4, which was about two times lower than other simulations found in the literature. To describe the global selectivity, a simple approach combining the CEL model and the average ratio of diffusion coefficients was proposed, resulting in a selectivity of around 1.

1. Introduction

The generic term *kerogen* refers to the solid organic matter found in sedimentary source rocks (shales, coal beds). These unconventional fossil fuel reservoirs have developed rapidly over the last two decades. Shale gas, in particular, has led to numerous applied research projects [1]. This spectacular development has been slowed down in recent years by the awareness of the impact of fossil fuels on global warming by public decision makers. Nonetheless, since natural gas is the fossil resource that emits the least amount of carbon dioxide (CO₂) per unit of energy produced (e.g. almost 50% less than coal and 30% less than home heating fuel [2]), it is considered as a transitional energy in the expectation of a rapid development and diversification of renewable energy sources. Therefore, in this context of an ever-changing energy mix, the understanding of the physical mechanisms implied in gas production from gas shales or coal beds remains an important issue, especially in order to reduce its environmental impact. In this respect, the injection of CO₂ should be considered as a way to improve the recovery of natural gas while improving its carbon footprint [3].

Kerogen is a nanoporous material containing a large proportion of micropores (i.e., with pore size below 2.5 nm following IUPAC standards), close to synthetic amorphous carbons from the point of view of its molecular structure, in which hydrocarbon fluids, and notably natural gas, have been naturally generated and stored over geological time [4,5]. In source rocks mature enough to have generated hydrocarbon fluids, kerogen represents at best about 5% of the total rock weight. Nevertheless, it is in the kerogen nodules embedded and disseminated in the mineral matrix that the majority of the gas in place (GIP) is stored due to adsorption [6–9]. Some authors estimated the contribution of sorbed gas to be roughly 50–60% of the total GIP [10,11], when others considered a wider range (20–80%) as more reasonable [12]. Therefore, understanding the adsorption and diffusion of gas mixtures in shales necessarily involves studying these mechanisms at the nanoscale of the kerogen.

While sorption capacity can be estimated from sorption isotherm experiments on isolated kerogen samples [13], the very heterogeneous structure of the shales does not allow the extraction of kerogen in the form of monolithic samples, making it almost impossible to study fluid

* Corresponding author.

E-mail address: romain.vermorel@univ-pau.fr (R. Vermorel).

<https://doi.org/10.1016/j.fuel.2023.129020>

Received 18 February 2023; Received in revised form 10 June 2023; Accepted 15 June 2023

Available online 27 June 2023

0016-2361/© 2023 Elsevier Ltd. All rights reserved.

transport in kerogen experimentally. Mainly because of these technical difficulties, many approaches have been proposed to develop molecular models of kerogen for use in molecular simulations [14]. Since then, molecular simulation techniques have been widely used to characterize the behavior of fluids in a variety of kerogen models, which can represent different origins of organic matter (classified as kerogen type) and degrees of maturation. Numerous studies have focused on the simulation of alkane adsorption, mainly by the Grand Canonical Monte Carlo (GCMC) technique (e.g., [15–18]). In this regard, the results obtained on adsorption in micropores show that the simulated data are consistent with type I adsorption isotherms. From the perspective of simulating fluid transport through the kerogen, several works based on Molecular Dynamics (MD) simulations have highlighted the diffusive nature of the flows [19–21], which is not well-captured by classical Darcy models. These works agree that the collective diffusion coefficient of alkane molecules reduces to their self-diffusion coefficient. To a good approximation, the latter is inversely proportional to the length of the alkane chain and decreases with the total amount of fluid adsorbed in the kerogen.

In the context of enhanced natural gas recovery by injection of CO₂ into shales, many studies have also relied on the use of molecular simulations to investigate CO₂/CH₄ mixtures in various types of kerogen [22–28]. Several studies have also investigated the influence of moisture content on selective adsorption of CO₂/CH₄ mixtures [9,26,29,30]. The works that focused on the microporous matrix of kerogen (i.e. without the presence of pores larger than 2.5 nm in diameter), all show a selective adsorption that favors CO₂. In particular, some of these studies, which rely on GCMC techniques to calculate adsorption isotherms, show that the selectivity is more or less sensitive to pressure depending on kerogen type and moisture content [9,24,26,29]. Concerning the separation by diffusion, most of the works found in the literature are restricted to the calculation of the self-diffusion coefficients of each species and found CO₂/CH₄ diffusivity ratio in the range 0.6–0.9 [22,26]. Most of the aforementioned studies use molecular simulations to produce data that are supposed to substitute for real experiments, which are difficult to perform as explained above. To our knowledge, there is no work proposing models to predict the selectivity of kerogen towards CO₂/CH₄ mixtures. For more exhaustive information on existing kerogen molecular models and their use in molecular simulations for the calculation of mechanical properties, adsorbed quantities, transport properties and their couplings, the reader is referred to the recent review by Obliger et al. [14].

This work focuses on modeling the adsorption and diffusion of CO₂/CH₄ mixtures in mature type-II kerogens, typical of those encountered in gas shales [31]. Our study employs molecular dynamics simulations to document the mechanisms involved at the scale of kerogens micropores. The selectivity of kerogen towards CO₂/CH₄ mixtures for a wide range of compositions, pressures and temperatures has been studied under several aspects: (i) equilibrium competitive adsorption; (ii) non-equilibrium competitive adsorption when the kerogen sample is subjected to a steady-state pressure gradient; (iii) competitive diffusion under these same steady-state conditions. Our goal is to propose a simple formal framework, capable of describing selectivity in the three situations described above and easy to implement in larger scale models. For this purpose, we compare the adsorption selectivities predicted by two classical models, namely the Extended Langmuir (EL) and Loading Ratio Correlation (LRC) models, to our simulation data produced by means of the Dual Control Volume-Grand Canonical Molecular Dynamics (DCV-GCMD) technique. In order to improve the predictions, we propose a correction of the EL model by including a Redlich–Kister type correlation in order to reproduce the composition of the adsorbed phases as well as possible. With the same simulation technique, we then explore non-equilibrium conditions by subjecting the fluids to pressure gradients applied across the kerogen membrane. In particular, we discuss the influence of the flow on the selective

adsorption. Finally, from the direct calculation of the gas permeabilities, we infer the collective diffusion coefficients of each species in the mixture. The competitive adsorption/diffusion is then analyzed in the light of the obtained ratio of diffusion coefficients and the proposed adsorption model.

2. Methods

2.1. Molecular model of a mature, microporous kerogen

The way kerogen is generated in nature makes it impossible to solely derive a single, true structure theoretically [4]. Over the past two decades, several molecular structures were developed on the basis of experimental data [4,5,17,31]. Here, we employed an emerging approach [32], where kerogen macromolecules are used as basic units to generate larger porous models. This versatile approach offers a good control of the geochemistry, but requires a priori on kerogen macromolecules. It departs from data-driven approaches [17], where the generation of large molecular models is directly guided by structural, experimental data. There is no a priori on the final molecular structure, but it is not versatile. We considered a macromolecule of mature, type-II kerogen exhibiting properties corresponding to the gas window and referenced as type-IID in the work of Ungerer et al. [31]. The chemical composition is C₁₇₅H₁₀₂O₉N₄S₂ (i.e., H/C = 0.58, O/C = 0.051, N/C = 0.023, and S/C = 0.011) [31]. 5 kerogen macromolecules and 25 methane molecules (5 CH₄/macromolecule) were randomly inserted in an initial cubic simulation box of 10 × 10 × 10 nm³ (see the supplementary material for more details). Methane molecules were used to increase the porosity of the final molecular structure. Using LAMMPS¹ [33] and an all-atom force field (pcff) [34], we performed MD to equilibrate the system during 250 ps at 1000 K in the canonical ensemble (i.e., the number of atoms (*N*), the volume (*V*), and the temperature (*T*) are constant) with a time step of $\delta t = 1$ fs. This first step was followed by successive runs of 300 ps at a pressure *p* = 20.27 MPa in the isothermal–isobaric ensemble (i.e., the number of atoms (*N*), the pressure (*p*), and the temperature (*T*) are constant) to decrease the temperature from 900 to 300 K with a temperature interval of $\Delta T = 200$ K. Prior to perform the last simulation at 300 K, methane molecules were removed from the molecular model. Temperature and pressure were maintained in the simulation box using a Nosé–Hoover thermostat [35,36] and a Parrinello–Rahman barostat [37] with relaxation times of 0.1 ps and 1 ps, respectively. We employed the P³M technique [38] to compute Coulomb interactions with a relative error in forces (i.e., accuracy) set to 10^{−5}. The cutoff radius for Lennard–Jones and real-space Coulomb interactions was set to $R_{\text{cut}} = 1.2$ nm. The final molecular structure was enclosed in a simulation box of 2.71 × 2.71 × 2.71 nm³ meaning that the model under consideration has a mass density of 1.03 g/cm³, a porosity of ~6.5% (i.e., $V_p \sim 1.29$ nm³), a specific surface area of 66.98 m²/g, and pore radii ≤ 1 nm, i.e., below the mesoporosity limit (see Fig. 1) [39]. The final mass density of our model lies in the range of experimental values, i.e., 0.9–1.4 g/cm³ [14]. Average and median pore radii were found to be 0.3706 and 0.3944 nm, respectively. As in the work of Collett et al. [32], porosities and specific surface area were determined by employing the algorithms of Herrera et al. [40] and Bhattacharya et al. [41], respectively, and by using a methane probe having a diameter of 0.3691 nm as defined in the COMPASS force field [34].

From the previously generated molecular structure of mature, microporous kerogen, we duplicated the porous model and translated it by 10 nm along the *x*-direction in order to create a reservoir in between them. A second reservoir was added along the same direction in a way that each molecular structure is directly in contact with the two reservoirs through periodic boundary conditions. The whole system is

¹ We used the November 2016 version.

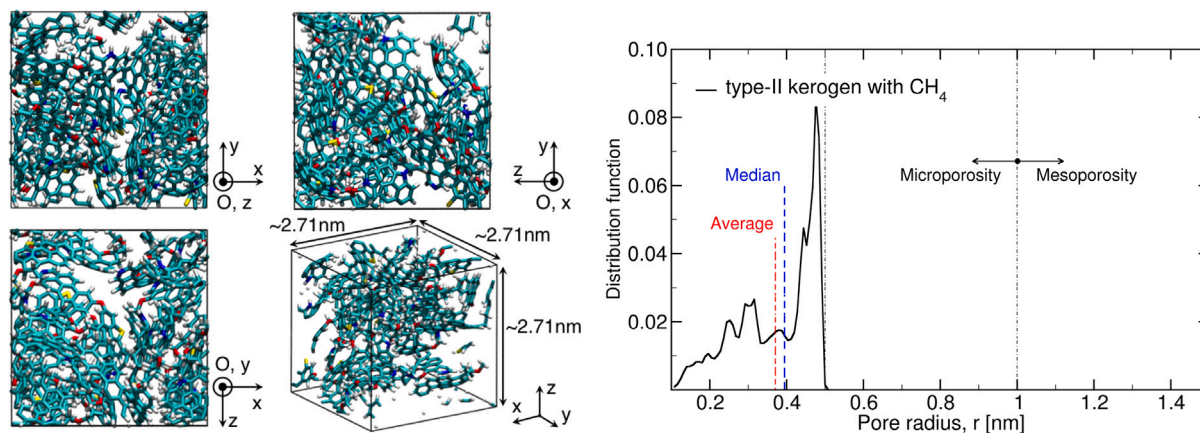


Fig. 1. (left) Snapshots showing the mature, microporous molecular model of kerogen; green, white, red, blue, and yellow licorices stand for carbon, hydrogen, oxygen, nitrogen, and sulfur atoms, respectively; (right) Resulting pore size distribution of the molecular structure. Blue and red vertical lines stand for the median and the average pore size, respectively. (For interpretation of the references to color in this figure legend, the reader is referred to the web version of this article.)

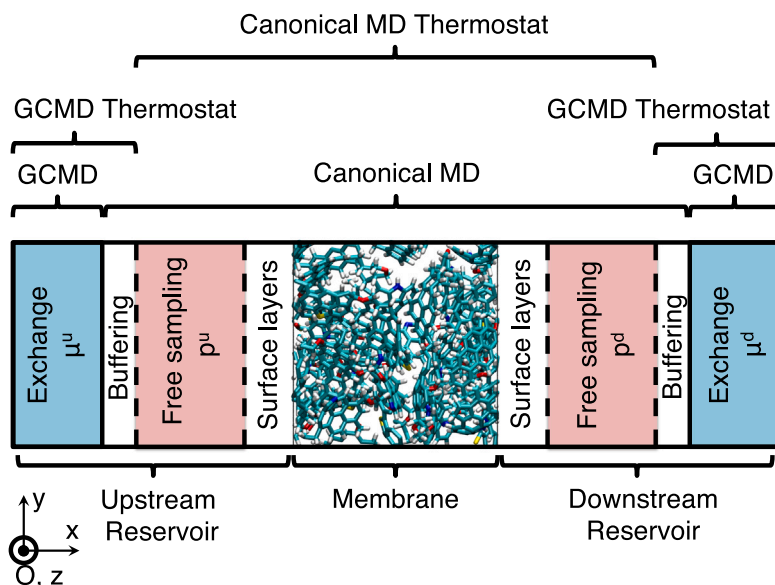


Fig. 2. Design of the simulation box for the study of equilibrium and transport properties. The chemical composition of the fluid is controlled through the exchange regions (i.e., chemical potentials μ_u , μ_d), while the free sampling regions are employed to monitor bulk properties (e.g., pressures p_u , p_d) in a perturbation-free zone. Equilibrium properties were computed for $\mu_u = \mu_d$, while transport properties were computed for $\mu_u \neq \mu_d$ (i.e., gradient of chemical potential). Half of the simulation box is shown along the x -direction in this figure. Location of regions in the other half of the simulation box are symmetrical with respect to the (O, \vec{y}, \vec{z}) plane.

enclosed in a simulation box of $\sim 25.42 \times 2.71 \times 2.71 \text{ nm}^3$. A sketch of half of the simulation box is shown in Fig. 2. This kind of simulation box design is similar to previous ones employed in the literature for the study of transport properties [42–46].

2.2. Simulations for equilibrium and transport properties

In this work, we were interested in CH_4 and CO_2 mixtures adsorbed in mature, microporous kerogen under a wide range of thermodynamic conditions. In the following of this paper, parameters with subscript $i = 1$ refer to methane, while those with subscript $i = 2$ refer to carbon dioxide. We considered various chemical compositions of the fluid from pure CH_4 (bulk molar fraction of $x_1 = 1$) to pure CO_2 ($x_1 = 0$) with a step of 0.1 at 350, 400, and 450 K. Given the average geothermal gradient (25–30 K/km) and the surface temperature ($T_{\text{surf}} = 288.15 \text{ K}$) [47], our simulation temperatures correspond to geological depths (h_{geol}) in the range 2.1–6.5 km, which partly overlaps field conditions for shales (~ 1.5 –3 km). Given the hydrostatic pressure gradient, our

chosen temperatures and their corresponding geological depths constrained our study to a pressure range 0–60 MPa. In our study, we staid limited to $p \leq 35 \text{ MPa}$. Thermodynamics conditions considered here are comparable to previous simulation works on kerogen (298.15–353 K and ~ 0.1 –30 MPa) [23,31,32,48–53]. We have deliberately chosen not to study temperatures lower than 350 K, because at the approach of its critical point, the CO_2 tends to reach quasi-liquid densities at the interface between the kerogen and the bulk reservoir. In our dynamic simulations, this effect would impair the analysis of the results because we would have to decouple the surface effects (at the entrance and exit of the kerogen membrane) from the mechanisms acting in the kerogen volume.

In our approach, methane and carbon dioxide molecules were free to move in the course of the simulation, whereas kerogen membranes were kept frozen. We employed the all-atom force field pcff [34] as implemented in LAMMPS [33] to describe intra- and intermolecular interactions among methane and carbon dioxide molecules as well as interactions between the frozen, kerogen substrate and the fluid

(i.e., dispersion–repulsion parameters and partial charges only). We used the P³M technique [38] to compute Coulomb interactions with a relative error in forces set to 10^{-5} . The cutoff radius for Lennard-Jones and real-space Coulomb interactions was set to $R_{\text{cut}} = 1.2$ nm. Periodic boundary conditions were used in the three directions of space.

Then, equilibrium and transport properties were computed using Dual Control Volume-Grand Canonical Molecular Dynamics (DCV-GCMD) [54] as enabled in LAMMPS [33]. This technique in combination with the simulation box we designed necessitated the definition of spatial regions (see Fig. 2). In reservoirs and far from kerogen membranes, we set up two exchange regions, each having a width of 5 nm, where the chemical composition of the fluid is constrained using a Monte Carlo routine that inserts and deletes molecules in order to equilibrate chemical potentials related to each region, namely μ^u and μ^d in Fig. 2. Without taking care, inserting flexible molecules whose internal degrees of freedom are not in thermal equilibrium can ruin the dynamics by making the temperature inhomogeneous. In that regard, we modified the grand canonical Monte Carlo (GCMC) routine from its original LAMMPS version in order to improve insertion and deletion of small, flexible molecules, by adjusting the initial velocities of their individual atoms so that the equipartition of the energy between the different degrees of freedom is reached more quickly. A velocity vector of the center of mass of the molecule is generated by respecting the Maxwell Boltzmann equilibrium velocity distribution at the target temperature. Independently, initial velocities for individual atoms are generated following the same procedure but with an amplitude multiplied by a $\sqrt{\alpha_T}$ prefactor, and then globally corrected so that the center-of-mass velocity generated at first is restored. Simulations of bulk gas mixtures in the temperature range 350–450 K show that the intramolecular energies obtained in the NVT ensemble are recovered by tuning this prefactor with values of the order of $\alpha_T \sim 18$ for CH₄ and $\alpha_T \sim 9$ for CO₂. Note that exchange regions in our work are called control volumes elsewhere [42,43,45,46,54]. While Monte Carlo rules were used for inserting or deleting molecules, translational and rotational molecular motions were carried out by integrating equations of motion (i.e., MD steps). In between kerogen membranes and exchange regions, four free sampling regions of a width 1.3 nm were defined allowing us computing bulk properties of the simulated fluid like pressure, namely p_u and p_d in Fig. 2. We used those computed quantities to compute the exact values of the pressures imposed on each sides of the membranes as slight discrepancies with the target pressure can be expected with the DCV-GCMD method [55]. Limits along the x -axis of those free sampling regions were chosen so that (i) they do not incorporate surface layers, i.e., regions of the fluid that are strongly affected by the presence of the kerogen substrate (~ 2 – 3 molecular diameters), and (ii) they are far enough from the exchange regions in order to avoid bias trajectories of molecules due to the insertion and the deletion of other molecules (i.e., buffering regions in Fig. 2). Widths of aforementioned regions were set to 1 nm for surface layers and 0.2 nm for buffering. For equilibrium simulations, we performed 1000 MC insertion and deletion trial steps every 20000 MD steps (i.e., 20 ps), meaning that the MC/MD ratio is 0.05. For the computation of transport properties, a higher MC/MD ratio of 0.2 was necessary to reach the steady state with pressure gradients (or gradient of chemical potentials) sufficiently close to their target values in the simulation box. These MC/MD ratios are rather low compared to what is practiced in other works [55], nevertheless we had to limit this ratio not to disturb the thermodynamic equilibrium of the reservoirs. Indeed, the insertion of flexible molecules in the course of MD simulations requires some time to reach an equipartition of the kinetic energy between the different intramolecular degrees of freedom, as discussed earlier. The main disadvantage of using low MC/MD rates is to impose a lower pressure gradient than expected. However, we circumvent this problem by directly calculating the pressures in the free sampling regions as explained above. Raw data from our simulations validating the proposed DCV-GCMD method are presented in supplementary material.

The whole volume but the exchange regions was set to the canonical ensemble. Thus, adsorption and desorption in porous matrices occur solely through the motion of molecules (kinetics) making this technique very useful, since, similarly to experiments, only the accessible porosity contributes to sorption processes. The temperature in the simulation box was maintained using two Nosé–Hoover thermostats [35,36] with a relaxation time of 0.1 ps: one for exchange and buffering regions, where the dynamics of molecules is perturbed by the insertion and the deletion of molecules, and the other one for the rest of the simulation box. MD trajectories were integrated using the velocity verlet integrator algorithm with a time step of 1 fs.

If, for equilibrium properties like adsorption isotherms, we set the same thermodynamics conditions in the two exchange regions (same chemical potentials, $\mu_i^u = \mu_i^d$, and temperatures, $T_u = T_d$), different conditions were set for transport properties (i.e., $\mu_i^u > \mu_i^d$ and $T_u = T_d$) generating a driving force (a gradient of chemical potential) at the origin of the mass transfer. We considered three gradients of chemical potentials that correspond roughly to the following pressure gradients: ~ 2 , ~ 4 , and ~ 6 MPa/nm. Two sets of simulations were performed: one with a constant downstream pressure (~ 5 MPa) and one with a constant upstream pressure (~ 20 MPa). This allowed us assessing the combined effect of the pore filling and the pressure gradient. Runs to reach equilibrium or a steady state had at least a 2-ns length. Production runs had lengths in the range 2–25 ns with a sampling rate of 1 ps. To relate chemical potential of species (μ_i) with the chemical composition of the fluid (x_i), the temperature (T), the pressure (p), and the mass density (ρ_m), we performed preliminary bulk simulations. By fitting ad-hoc polynomial to the $p - \mu$ data of bulk mixtures, we derived correlations to help us compute the local chemical potentials (or fugacities) in the free sampling regions from the calculated pressures. Data and details are given in the supplementary material.

Furthermore, prior to study adsorption of methane/carbon dioxide mixtures in the temperature range 350–450 K, we assessed the effect of the temperature (i.e., thermal expansion) on the molecular structure. Preliminary simulations (reported in the supplementary material) showed that the linear strain in our systems due to the rise of the temperature does not exceed 1%. In this type of microporous material, though, the main source of deformation would result from adsorption-induced swelling if we let the membrane volume relax during our simulations. These deformation effects and their coupling to gas diffusion in kerogen is the subject of recent research [56]. Nevertheless the impact of these effects remains low for mature kerogen models such as the one studied in this paper [14] and we chose to disregard them by maintaining the kerogen structure rigid.

2.3. Uncertainty calculations and definitions of statistical estimators

Molecular simulations, like real life experiments, inherently generate scatter in the data resulting from thermal fluctuations. The uncertainties related to the calculation of adsorbed quantities, and especially to that of molar fluxes, in porous matrices as poorly permeable as kerogen are not negligible. In this study, we used the well-known block averages method to calculate the standard deviations on the raw data of the simulations such as the number of adsorbed molecules, the pressures and the molar fluxes [57]. For any quantity derived from analytical formulas involving these raw data, we used classical analytical error propagation calculations, which conservatively tend to overestimate the uncertainties by summing the relative errors of each term.

Moreover, we have performed different fits to compare our results to models or correlations, which requires a particular attention to the error propagation in the fitted parameters. All the fits performed in this work are based on the least squares method and use a weighting of the data points. The weight assigned to each point is inversely proportional to the associated standard deviation in order to limit the impact of the data with the worst statistics on the fitting results.

To estimate the uncertainty on the parameters fitted with nonlinear models, we used a customized bootstrap method [58]. For each dataset on which we perform a fit, we assume that each data point follows a Gaussian distribution with a standard deviation that matches that obtained by the block-average method or the analytical error propagation calculation discussed above. We then randomly generate virtual datasets based on this distribution and apply the fit to each of them to obtain a corresponding population of optimal parameters. The standard deviation of this set of optimal parameters gives us the error on the parameters fitted to the original dataset. To perform this calculation, we generated virtual datasets as long as the relative difference between the current estimate of the standard deviation and its value corrected by the addition of a new dataset exceeded 10%. To ensure that this criterion did not lead to non-convergent results, we imposed a minimum of 1000 virtual datasets.

To compare the fits of different models to our data, we used three estimators to measure the quality of fits. Specifically, for a dataset $\{X_j, Y_j\}$ with $j = 1, 2, \dots, n$ to which a theoretical model $Y = f(X)$ is fitted, we define the Relative Error (RE) with respect to the data point j as

$$\text{RE}(Y_j) = \frac{f(X_j) - Y_j}{|Y_j|}. \quad (1)$$

The Average Relative Error (ARE) of a fit to a whole dataset is defined as :

$$\text{ARE}(\{Y_j\}) = \frac{1}{n} \sum_{j=1}^n \frac{|f(X_j) - Y_j|}{|Y_j|}, \quad (2)$$

and its Maximum Absolute Deviation (MAD) reads

$$\text{MAD}(\{Y_j\}) = \max_{\{j\}} \frac{|f(X_j) - Y_j|}{|Y_j|}. \quad (3)$$

3. Competitive adsorption at equilibrium

Fig. 3 shows the adsorption isotherms of CH_4/CO_2 mixtures as well as pure species at equilibrium obtained by maintaining homogeneous chemical potentials in each reservoir of our simulation box. Here, we represent the results obtained in terms of moles of adsorbed gas per unit mass of Total Organic Carbon (TOC), where the mass of TOC is simply the mass of the solid matrix in our case. This unit is commonly encountered in experimental studies because it relates the adsorbed amounts to the mass of the adsorbent (kerogen) contained in the shale samples analyzed, making it possible to compare adsorption data from samples of varying origins. Quantitatively, our results obtained for the adsorption of pure species are comparable to the experimental measurements found in the literature (see the supplementary material for more details). Therefore, we will use this unit when referring to fluid concentration, also referred to as fluid loading, in the rest of this paper.

The data reported in Fig. 3 follow the usual Langmuir shape observed in this type of microporous amorphous carbons [14,59]. Before analyzing these isotherms in more details, let us first look at the composition of the adsorbed phases. Fig. 4 shows parity plots comparing the compositions of the adsorbed and bulk phases. Presented in this way, our simulation results highlight that CO_2 adsorbs preferentially to CH_4 inside our kerogen model. Indeed, in the absence of selective adsorption, the compositions of the adsorbed and bulk phases would be identical and the adsorbed mole fractions, y_1 and y_2 (subscript $i = 1$ refers to CH_4 while $i = 2$ refers to CO_2), would simply be equal to the bulk mole fractions, x_1 and x_2 , and would appear as straight lines of equations $y_1 = x_1$ and $y_2 = 1 - x_1$ in the diagrams of Fig. 4. Our data however deviate significantly from this ideal behavior since the parity curves show a marked curvature, especially for mole fractions of methane in the bulk $x_1 \gtrsim 0.5$. We clearly observe that the adsorbed mole fraction of CH_4 is lower than its bulk value, and conversely we

Table 1

Parameters computed from the fit of our simulation data plotted as a function of the bulk pressure (p) with the Langmuir model and the Loading Ratio Correlation (LRC) model.

Species	T [K]	Langmuir model		LRC model		
		$N_{s,l}$	b_l [1/MPa]	$N_{s,lrc}$	b_{lrc} [1/MPa]	η
CH_4	350	57 ± 2	0.29 ± 0.03	70 ± 10	0.24 ± 0.05	0.8 ± 0.1
	400	58 ± 5	0.13 ± 0.03	64 ± 9	0.14 ± 0.01	0.9 ± 0.1
	450	52 ± 7	0.11 ± 0.03	60 ± 10	0.10 ± 0.01	0.82 ± 0.09
CO_2	350	70 ± 1	0.57 ± 0.05	80 ± 20	0.6 ± 0.1	0.7 ± 0.6
	400	65 ± 3	0.27 ± 0.05	70 ± 20	0.29 ± 0.08	0.9 ± 0.4
	450	58 ± 3	0.18 ± 0.04	60 ± 30	0.19 ± 0.03	0.8 ± 0.4

observe the opposite trend for CO_2 . This behavior is typical of non-ideal mixtures.

In order to describe this selective adsorption, we first propose to use some adsorption models found in the literature. Different analytical adsorption models can be used to reproduce the isotherms of pure species. In this study, we used the Langmuir model and the Loading Ratio Correlation (LRC) model commonly used to describe adsorption in microporous materials [59,60]. The Langmuir isotherm corresponds to the following equation:

$$N = N_{s,l} \frac{b_l p}{1 + b_l p}, \quad (4)$$

where $N_{s,l}$ is the maximum number of adsorption sites (or maximum capacity of the monolayer), $b_l = 1/p_L$ is the inverse Langmuir pressure, i.e., the pressure at which the adsorbed layer (monolayer) reaches half of its capacity, and p is the gas pressure (bulk). Petroleum engineers classically assess sorption capacity of shales with the Langmuir model because of its simplicity and its sound physical foundation. The LRC model applied to pure component adsorption is written as [60]:

$$N = N_{s,lrc} \frac{b_{lrc} p^\eta}{1 + b_{lrc} p^\eta}, \quad (5)$$

where η is an additional degree of freedom supposed to account for the spread of the energy distribution at the surface of heterogeneous adsorbents. We fitted each of these two models to the adsorption isotherms of the pure species and the optimized parameters are reported in Table 1. For a reason that will be explained later, we have shown only the curves obtained with the Langmuir model in Fig. 3.

Now that we have estimated the parameters of these models for pure components, we can extrapolate to the case of binary mixtures CH_4/CO_2 . The Langmuir parameters can be injected into the classical Extended Langmuir (EL) model which is written as follows [61]:

$$N_i = N_{i,s,l} \frac{b_{i,l} p_i}{1 + b_{1,l} p_1 + b_{2,l} p_2}, \quad (6)$$

where subscript i stand for species under consideration. The partial pressure of species i is defined as $p_i = x_i \times p$, x_i being the mole fraction of species i in the bulk. Similarly, the LRC model applied to binary mixtures is defined as [60]:

$$N_i = N_{i,s,lrc} \frac{b_{i,lrc} p_i^{\eta_i}}{1 + b_{1,lrc} p_1^{\eta_1} + b_{2,lrc} p_2^{\eta_2}}, \quad (7)$$

Rather than comparing these models directly to the adsorption isotherms or compositions of adsorbed phases reported in Figs. 3 and 4, we prefer to investigate what they predict in terms of selectivity. Selectivity (or separation factor) is commonly used to characterize competitive adsorption [9,47] and in the context of this work the selectivity of CO_2 vs. CH_4 due to adsorption is defined as:

$$S_{2/1}^{\text{ads}} = \frac{y_2}{x_2} \times \frac{x_1}{y_1}, \quad (8)$$

where we recall that y_i and x_i denote the molar fraction of compound i in the adsorbed and bulk phases respectively. While the adsorption

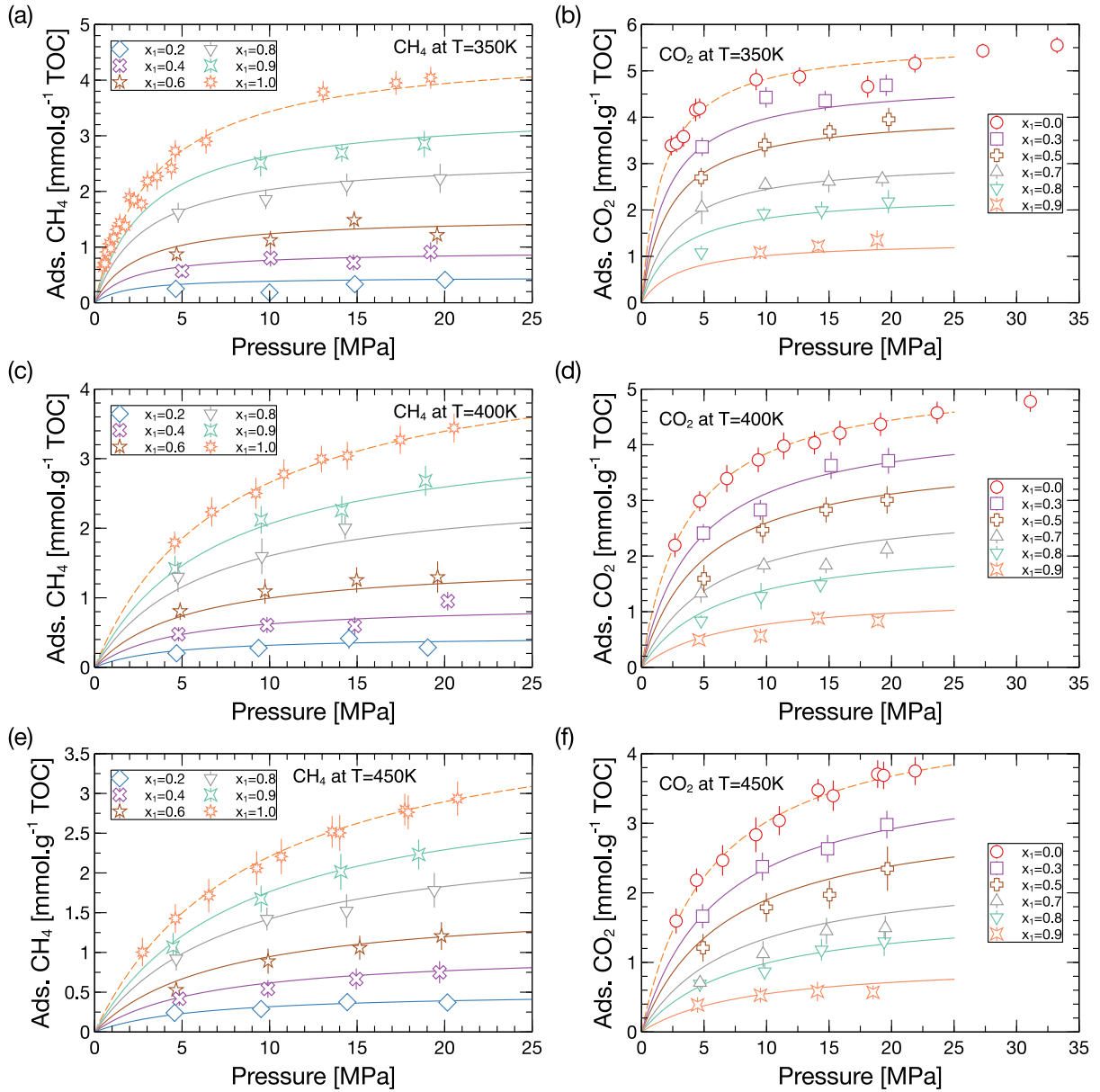


Fig. 3. Adsorption isotherms of methane and carbon dioxide mixtures in a membrane of mature, microporous kerogen plotted as a function of the pressure in the reservoir, p (i.e., the bulk pressure) at 350 K (a–b), 400 K (c–d), and 450 K (e–f). Open symbols represent data obtained for a wide range of molar fractions of methane in the bulk, x_1 . Lines with matching colors stand for the fitted theoretical models. Dashed lines stand for the fit of the Langmuir isotherm model to the adsorption isotherms of the pure species. Solid lines stand for the fits of the Corrected Extended Langmuir model to the adsorption isotherms of the mixtures. (For interpretation of the references to color in this figure legend, the reader is referred to the web version of this article.)

models discussed above may give qualitatively similar trends for adsorbed amounts, study of the predicted behavior for selectivities reveals fundamental differences. First, the EL model predicts a selectivity independent of pressure and mixture composition, determined solely by the Langmuir parameters of the pure species:

$$S_{2/1,el}^{ads} = \frac{N_{2,s,l} b_{2,l}}{N_{1,s,l} b_{1,l}}. \quad (9)$$

On the other hand, because of the additional exponent on partial pressures, the LRC model yields a composition- and pressure-dependent selectivity according to the following equation:

$$S_{2/1,lrc}^{ads} = \frac{N_{2,s,lrc} b_{2,lrc}}{N_{1,s,lrc} b_{1,lrc}} \times p^{\eta_2 - \eta_1} \times \frac{(x_1)^{1-\eta_1}}{(1-x_1)^{1-\eta_2}}. \quad (10)$$

This analytical form then produces a selectivity that tends to 0 as x_1 approaches 0 and diverges as x_1 approaches 1, which is an unphysical behavior. Fig. 5 shows the CO_2/CH_4 selectivities deduced from the simulations of binary mixtures adsorption in our kerogen model. Despite large error bars due to the accumulation of uncertainties in the selectivity calculations, in accordance with what is shown in Figs. 3 and 4 we observe a selective adsorption in favor of CO_2 with $2 \lesssim S_{2/1}^{ads} \lesssim 4$.

These values are close to experimental ones (2.565–4.166) obtained on Sichuan Basin shales (Nanchuan) in the temperature range 278–318 K [62]. Our values are also close to previous simulations on molecular models of type-I kerogen (~2–4) [9,24], type-II kerogen (~3–6) [9], and type-III kerogen (~4–7) [9] in the temperature range 338–388 K. Globally, if we can conclude that this selectivity decreases with temperature, we do not observe any notable effect of the reservoir

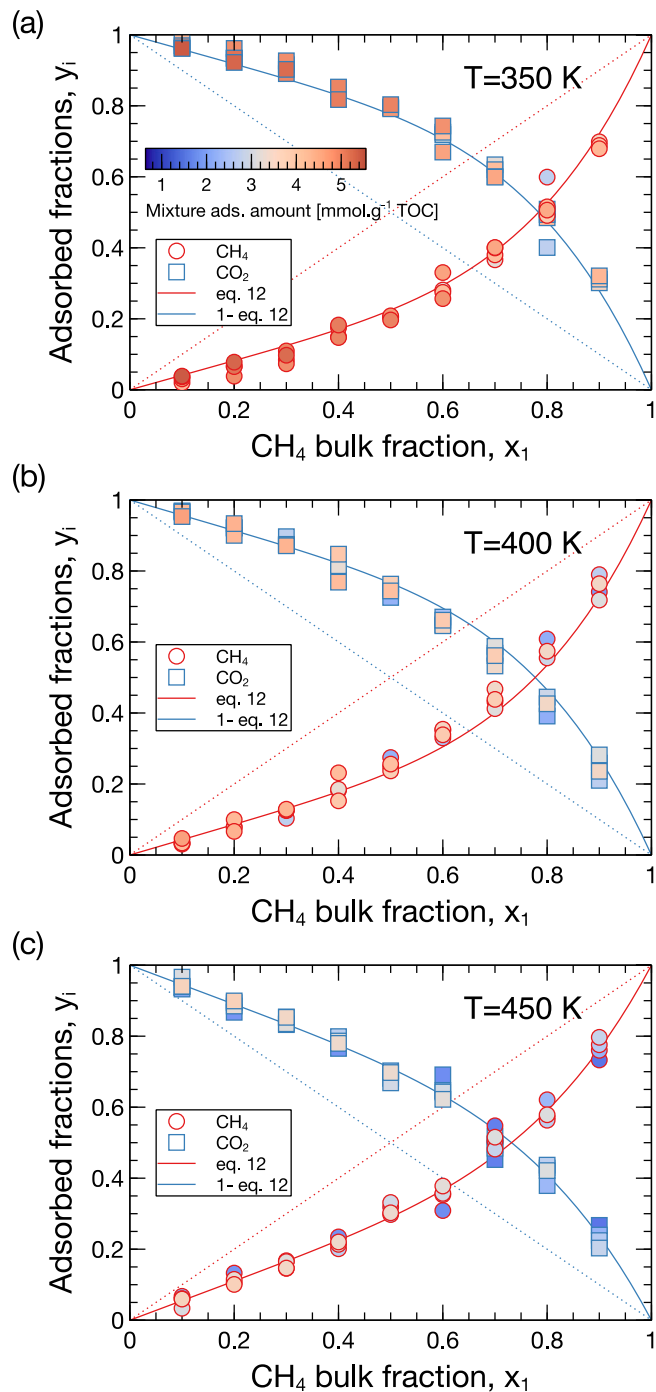


Fig. 4. Mole fractions in the adsorbed phase, y_i , plotted as a function of CH_4 bulk mole fraction, x_1 , at 350 K (a), 400 K (b), and 450 K (c). Circles and squares symbols stand for simulation data obtained for CH_4 and CO_2 , respectively. All symbols are colored with respect to the total adsorbed amount in the kerogen membranes according to the colormap shown in subfigure (a). The red solid line and blue solid line stand for the fit of the CEL model proposed in this paper. Red and blue dotted lines stand for lines of equations $y = x$ and $y = 1 - x$ respectively. (For interpretation of the references to color in this figure legend, the reader is referred to the web version of this article.)

pressure (i.e. the fluid loading) and it is difficult, given the large error bars, to analyze precisely the dependence on the mixture composition. Our results are consistent with other simulations performed on kerogen structures based on the same type-IID kerogen model as used in this study [31], which show negligible pressure dependence above 6 MPa [26,29]. Other authors do however observe a significant pressure effect on selectivity, but their work deals with less mature kerogens structures [9,24]. Less mature kerogen usually have a higher proportion of heteroatoms, which can increase uptake of CO_2 and the sensitivity of selectivity to pressure [63]. The lack of pressure effect in our data can also be explained by our use of the DCV-GCMD technique which does not insert the fluid molecules directly into the kerogen. It is possible that studies based on random insertions of molecules into kerogen by the conventional GCMC method overestimate the adsorption of CO_2 at low pressure by providing access to otherwise inaccessible adsorption sites, which would explain the observed selectivity peak at low pressure. More specifically, significant occluded porosity corresponding to small pore sizes could increase the sensitivity of selectivity to pressure, as observed in simpler structures such as carbon nanotubes [64].

In Fig. 5 we have also reported the predictions of the different models discussed in this work. The LRC model predictions were calculated for reservoir pressures of 4 MPa and 20 MPa which correspond to the bounds of the pressure range studied for the mixture simulations. We immediately notice the incorrect shape of these curves with non-finite selectivity values at the limits of the bulk mole fraction interval $x_1 \in [0; 1]$, which, in our opinion, disqualifies the LRC model for predicting the selective adsorption of mixtures. With a molecular model of kerogen close to the one used in our work, Glantz et al. fitted several classical models to simulated adsorption isotherms for methane/ethane mixtures [65]. They came to the opposite conclusion that the LRC model was the most accurate. Nevertheless, to reach this conclusion, they directly fitted the LRC model parameters to the mixture data (i.e. the optimal parameters for the mixture are different from those found for the pure species). Most importantly, they did not discuss the inability of the LRC model to predict the selectivity of mixtures with highly asymmetric compositions.

As for the EL model, Fig. 5 shows that it tends to systematically underestimate selectivity by as much as 40% compared to the averaged data points (marked by black squares). Most likely, the classical EL model based on purely energetic arguments fails to capture the entropy effects that accompany the adsorption of mixtures of molecules exhibiting unlike geometric properties. Although these entropy effects are probably less dramatic than in crystalline adsorbents [66], we believe they are largely responsible for the discrepancies observed between our simulation data and the predictions of the classical EL model. For mixtures where each component exhibit comparable adsorbed quantities at saturation of the pure gas phase (single component), which is rather the case in our simulation conditions, species having the smallest size or the most favorable aspect ratio should adsorb in greater quantity [67].

Rather than going into theoretical considerations to include these effects in the mixture adsorption modeling, we propose a simple empirical approach to correct the EL model and improve its predictions. More precisely, we remark in Fig. 4 that the excess mole fraction of methane in the adsorbed phase could be represented by an empirical equation of the form $y_1 - x_1 = \alpha(x_1^\gamma - x_1)$ where the parameters α and γ remain to be determined. This ad hoc equation is reminiscent of the Redlich–Kister polynomials commonly used to describe excess functions in mixture thermodynamics [68]. Instead of simply fitting these additional parameters to our data, we propose to include this correlation in the classical EL model and to impose some constraints to reduce the number of degrees of freedom.

In the following, we derive the equations describing the Corrected Extended Langmuir (CEL) model that we propose in the case of a binary mixtures where compound 2 adsorbs preferentially to compound 1. The adsorbed amount of compound i is written as

$$N_i = N_{i,s,cel} \frac{b_{i,l} p_i}{1 + b_{1,l} p_1 + b_{2,l} p_2}, \quad (11)$$

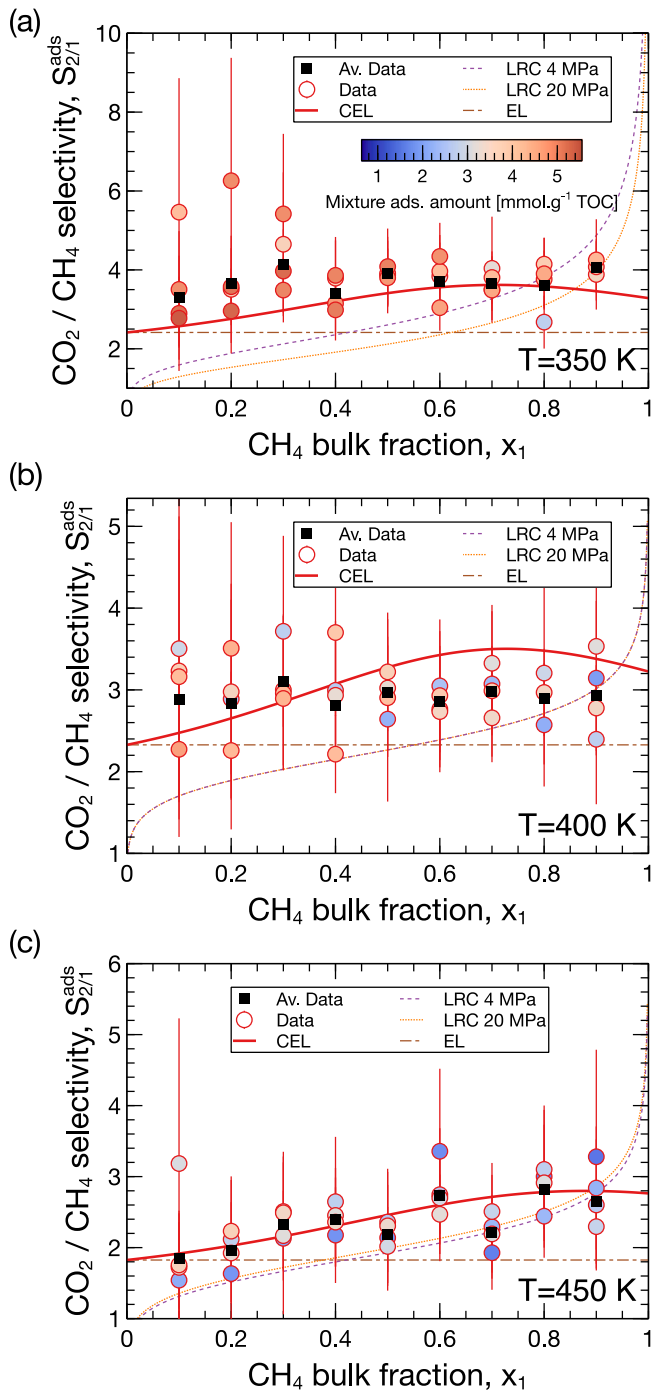


Fig. 5. CO₂/CH₄ selectivity due to adsorption, plotted as a function of CH₄ bulk mole fraction, x_1 , at 350 K (a), 400 K (b), and 450 K (c). Circles stand for simulation data. Symbols are colored with respect to the total adsorbed amount in the kerogen membranes according to the colormap shown in subfigure (a). Black squares stand for the weighted average of the data obtained at each value of x_1 , with weights set proportional to the inverse of the data uncertainties. The red solid lines stand for the predictions of the CEL model proposed in this paper. The orange dashed-dotted lines stand for the prediction of the EL model. The green and purple dotted lines stand for the predictions of the LRC model at reservoir pressures of 4 MPa and 20 MPa respectively. (For interpretation of the references to color in this figure legend, the reader is referred to the web version of this article.)

where $N_{i,s,cel}$ is a function of the composition x_i of the bulk binary mixture, and is different from the adsorbed amount of the pure compound i at saturation, $N_{i,s,l}$, deduced from the Langmuir isotherm. Based on the empirical formula introduced in the previous paragraph, we assume that the fraction of compound 1 in the adsorbed phase satisfies

$$y_1 = \alpha x_1^\gamma + (1 - \alpha)x_1, \quad (12)$$

where α and γ must satisfy the constraints $\alpha > 0$ and $\gamma > 1$ to reproduce the expected behavior (i.e. the same curvature as observed in Fig. 4). The aforementioned correlation and Eq. (11) result in the following expressions for the selectivity:

$$S_{2/1}^{\text{ads}} = \frac{y_2}{x_2} \times \frac{x_1}{y_1} = \frac{N_{2,s,cel} b_{2,l}}{N_{1,s,cel} b_{1,l}}. \quad (13)$$

By combining the Eqs. (12) and (13) we can write the selectivity as a function whose only variable is the molar fraction of compound 1 in the bulk:

$$S_{2/1}^{\text{ads}} = \frac{1 + (\alpha - 1)x_1 - \alpha x_1^\gamma}{(1 - x_1)(1 - \alpha + \alpha x_1^{\gamma-1})}. \quad (14)$$

This function is well-behaved at the limits of the interval $x_1 \in [0; 1]$ (see Appendix A for the detailed calculations), with the following boundary values

$$S_{2/1}^{\text{ads}}(x_1 = 0) = \frac{1}{1 - \alpha} \quad (15)$$

$$S_{2/1}^{\text{ads}}(x_1 = 1) = 1 + \alpha(\gamma - 1),$$

which provides an upper limit for α , since it must verify $0 < \alpha < 1$ to yield finite selectivity values greater than 1 (i.e. compound 2 must adsorb preferentially). The parameterization of α and γ then offers many possibilities to adjust the shape of the selectivity described by Eq. (14), discussed in detail in Appendix A. However, our approach consists in simplifying the parameterization of this correlation in a pragmatic way by reducing the number of adjustable parameters, even if it means losing precision.

In particular, the detailed study of the function $S_{2/1}^{\text{ads}}$ in the interval $x_1 \in [0; 1]$ shows that the selectivity is either a monotonic function or it passes through a maximum. We can therefore go one step further by considering that the boundary conditions must be imposed so that the selectivity remains higher than the one predicted by the EL model, taken as a lower bound. This leads to the following conditions on the model parameters:

$$\alpha \geq 1 - 1/S_{2/1,el}^{\text{ads}} \quad (16)$$

$$\gamma \geq 1 + S_{2/1,el}^{\text{ads}}.$$

Since species 2 adsorbs more, the minimum selectivity is itself greater than 1, so that in practice $\gamma \geq 2$. The closure of this model is then based on the following arbitrary constraints:

1. since our results suggest that the selectivity predicted by the classical EL model best approximates our data when $x_1 \rightarrow 0$ (see Appendix A), we match the selectivity of the CEL model to that of the EL model when $x_1 \rightarrow 0$;
2. When $b_{i,l} p \gg 1$, i.e., at saturation, we match the total adsorbed amounts (compounds 1 and 2 combined) of the CEL model to that of the EL model. This means that we assume that EL correctly predicts the maximum fluid loading, but not the composition of the adsorbed phase.

To apply the first condition, we may consider $x_1 \rightarrow 0$ in Eq. (13) to obtain

$$\alpha = 1 - \frac{N_{1,s,l} b_{1,l}}{N_{2,s,l} b_{2,l}}. \quad (17)$$

Therefore, α is completely determined by the Langmuir parameters of the pure compounds. The second condition yields

$$N_{i,s,cel} = [N_{1,s,l} b_{1,l} x_1 + N_{2,s,l} b_{2,l} (1 - x_1)] \frac{y_i}{b_{i,l} x_i}. \quad (18)$$

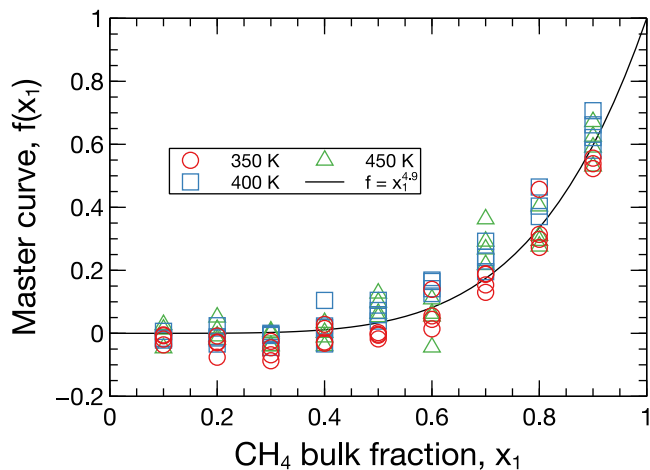


Fig. 6. f function, plotted as a function of CH_4 bulk mole fraction, x_1 . Red circles, blue squares and green triangles stand for simulation data obtained at 350 K, 400 K and 450 K respectively. The black solid line stands for the best fit of the $f(x_1)$ function predicted by the CEL model. The best fit was obtained with the parameter $\gamma = 4.9 \pm 0.3$.

Eqs. (11), (12), (17) and (18) constitute the proposed CEL model, which requires the exponent γ encountered in Eq. (12) as an additional parameter in comparison with the classical EL model. To fit the CEL model to our simulation data, we directly express the power law $f(x_1) = x_1^\gamma$ from the mole fraction of methane in the adsorbed phase as follows:

$$f(x_1) = x_1^\gamma = \frac{y_1^{\text{sim.}}}{\alpha} + (1 - \frac{1}{\alpha})x_1. \quad (19)$$

where the superscript “sim.” emphasizes the use of adsorbed compositions obtained from our simulations, and α must be computed by applying Eq. (17). We fitted Eq. (19) independently to our data obtained at temperatures of 350 K, 400 K and 450 K to yield the optimal γ values. The values produced are reported in Table 2. For our systems, we note that the γ values agree within the error bars for the three temperature values studied. To a good approximation, it seems that this parameter is independent of thermodynamic conditions. To test this hypothesis, we fitted the CEL model with a single value of the γ parameter for all three investigated temperatures. Fig. 6 shows that the simulation data collapses on the power law obtained with $\gamma = 4.9 \pm 0.3$.

Now that we have determined the optimal value of the γ parameter for our system, we can use the CEL model to calculate adsorption isotherms, compositions of adsorbed phases and adsorption selectivities. The CEL model predictions are shown as solid lines in Figs. 3, 4, 5. Overall, we observe a satisfactory agreement between the predictions of the CEL model and the simulation data regarding the adsorbed quantities. As revealed by the analysis of Relative Errors (RE) shown in Fig. 7 and the values of the Average Relative Errors (ARE) and Maximum Absolute Deviations (MAD) in Table 3, the CEL model captures much better the behavior of the adsorbed mixture. Indeed, the classical EL model tends to systematically overestimate the amount of the least adsorbed component, CH_4 in our case, and, conversely, to underestimate that of the most adsorbed component, CO_2 . As for the LRC model, if it performs correctly on the prediction of the adsorbed quantities of CO_2 , it greatly overestimates those of CH_4 . From the point of view of the compositions of the adsorbed phases and the selectivity, the CEL model brings a real added value compared to the EL and LRC models since its predictions are in satisfactory agreement with the simulation data, contrary to the two other models as discussed earlier.

4. Competitive transport and adsorption out of equilibrium

We now present the results obtained when the system is kept out of equilibrium and reaches a steady state regime by maintaining a

Table 2

γ and β parameters computed from the fit of our simulation data.

Parameter	Data set			
	350 K	400 K	450 K	All temperatures
γ	5.1 ± 0.3	4.7 ± 0.4	4.9 ± 0.4	4.9 ± 0.3
β	0.796 ± 0.006	0.886 ± 0.003	0.936 ± 0.002	–

Table 3

Average Relative Error (ARE) averaged over all mixture compositions and Maximum Absolute Deviation (MAD) between model predictions and CH_4/CO_2 mixtures adsorption isotherms computed for the Corrected Extended Langmuir (CEL) model proposed in this work, the Extended Langmuir (EL) model and the Loading Ratio Correlation (LRC) model.

Species	T [K]	ARE [%]			MAD [%]		
		CEL	EL	LRC	CEL	EL	LRC
CH_4	350	17	39	65	41	66	144
	400	8.3	20	33	21	32	76
	450	4.4	19	15	7.6	33	37
CO_2	350	4.1	13	7.2	11	32	12
	400	5.9	5.7	2.0	14	14	8.8
	450	4.2	8.8	6.6	17	25	11

constant pressure difference across the kerogen membrane, as described in Section 2. We imposed this pressure difference while maintaining a homogeneous bulk composition between the upstream and downstream gas reservoirs to make our non-equilibrium and equilibrium simulations comparable in terms of selective adsorption. We studied flows generated for various upstream and downstream reservoir pressures between about 4 MPa and 20 MPa. Thus we obtained results for different magnitudes of the pressure gradient and different values of the mean pressure, which allowed us to explore the effects of the driving force of the flow and the fluid loading inside the membrane.

These boundary conditions may seem counter-intuitive at first glance, since the scenario of injecting CO_2 into shale saturated with CH_4 corresponds more to a transient flow with inhomogeneous upstream and downstream pressures and compositions. However, it should be kept in mind that in our simulations (and classically in NEMD approaches of this type), the pressure gradients applied are of exaggerated amplitudes in order to obtain sufficient statistics for an acceptable simulation time, which poses no methodological problem as long as a linear flux/force relation is observed. Under real conditions, however, the gradients are several orders of magnitude smaller so that composition and pressure are almost homogeneous on a scale of a few nanometers. In the context of upscaling our simulation results to the scale of the gas shale reservoir (e.g. in macroscale reservoir simulations), where diffusion mechanisms in the kerogen would act on very large time scales in front of the Darcy-like flows occurring in the macropores (e.g. the natural or induced fracture network), it is thus very likely that a local equilibrium assumption could be used: pressure and composition would be considered uniform at the scale of an elementary volume and, a fortiori, at the scale of a kerogen nodule. In this context, the conditions imposed in our simulations are relevant.

As a first step, we can use the simulated molar fluxes to calculate the partial gas permeabilities of each species, P_{ei} , classically defined as

$$P_{ei} = \frac{J_i \delta}{p_i^u - p_i^d}, \quad (20)$$

where J_i is the norm of the molar flux per unit surface of species i , δ is the thickness of the kerogen membrane, and p_i^u and p_i^d are the upstream and downstream partial pressures of species i , respectively. The evolution of these partial permeabilities as a function of the molar fraction of methane in the bulk is shown in Fig. 8. The order of magnitude obtained, roughly in the range $0.2\text{--}6.5 \times 10^4$ barrer for CH_4 and $0.2\text{--}3.5 \times 10^4$ barrer for CO_2 , is comparable to those found in the literature for molecular models of amorphous carbons

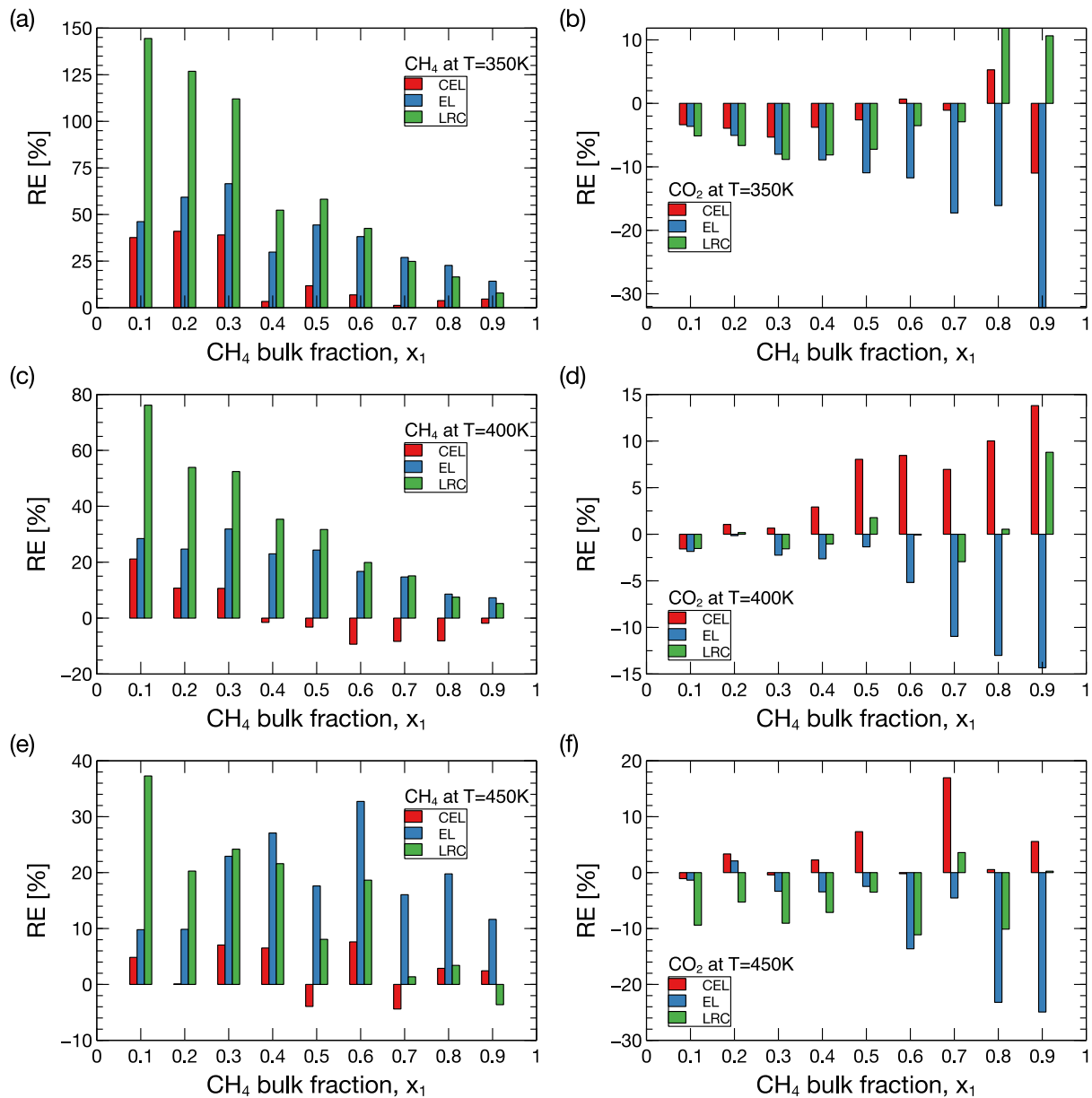


Fig. 7. Bar plots of the Relative Errors (RE) between the predictions of the different models and simulated CH_4/CO_2 mixtures adsorption isotherms, plotted as a function of CH_4 bulk mole fraction, x_1 . Results are shown for CH_4 at 350 K (a), 400 K (c), and 450 K (e), and for CO_2 at 350 K (b), 400 K (d), and 450 K (f). Red, blue and green histograms stand for the CEL, EL and LRC models respectively. (For interpretation of the references to color in this figure legend, the reader is referred to the web version of this article.)

of comparable density [46]. As expected, the partial permeabilities increase with the mole fraction of their respective compounds. In our system, we observe a crossing of the partial permeabilities of the two species for a molar fraction of bulk methane between 0.4 and 0.6. In particular, the intersection point shifts towards low methane fractions when the temperature increases. We observe no significant effect of the magnitude of the pressure gradient on the gas permeabilities (the size of the symbols in Fig. 8 is proportional to the pressure gradient). The influence of adsorbed fluid concentration is represented by the color of the data points in Fig. 8. Nevertheless, it remains difficult to interpret the influence of fluid loading on the transport of CH_4/CO_2 mixtures from these data because the permeability combines by definition the contributions, possibly coupled, of the concentration, c , and of the collective diffusion coefficient, D , since $J \propto cD$.

One way to decouple the effects of these two quantities is to use the formalism of Onsager's linear irreversible thermodynamics applied to mass transfer. Considering the transport of a binary mixture through

the membrane these equations are written:

$$\vec{J}_1 = -D_{11}c_1 \frac{\vec{\nabla}\mu_1}{RT} - D_{12}c_2 \frac{\vec{\nabla}\mu_2}{RT} \quad (21)$$

$$\vec{J}_2 = -D_{22}c_2 \frac{\vec{\nabla}\mu_2}{RT} - D_{12}c_1 \frac{\vec{\nabla}\mu_1}{RT} \quad (22)$$

where D_{11} and D_{22} are the auto-correlation Onsager's coefficients relating the molar flux of species 1 and 2 to their respective chemical potential gradients, D_{12} is the cross-correlation Onsager's coefficient relating the molar flux of a given species to the chemical potential gradient of the other species, μ_i is the chemical potential of species i , R is the ideal gas constant and T the temperature. Note that D_{ii} and D_{ij} are collective diffusion coefficients, related to the displacement of the centers of mass of each fluid species in response to the two chemical potential gradients. In our non-equilibrium simulations, although we impose chemical potentials in control zones, we do not have direct access to the chemical potential values in the immediate vicinity of the membranes. Nevertheless, we compute directly the values of partial

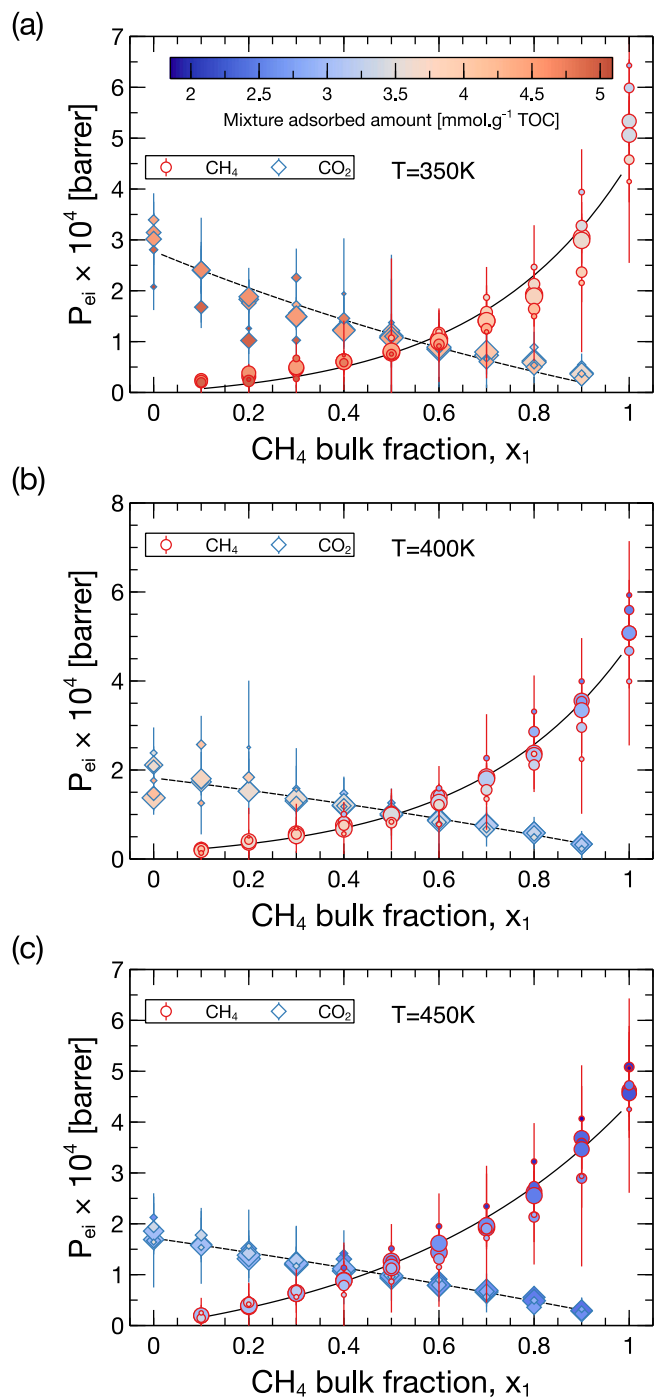


Fig. 8. Partial gas permeabilities of CH₄ and CO₂ in the mixture, plotted as a function of CH₄ bulk mole fraction, x_1 . Results are shown for 350 K (a), 400 K (b), and 450 K (c). Symbols stand for simulation data obtained according to Eq. (20). Symbol size scales with the amplitude of the global pressure difference ($p'' - p^d$) applied to the kerogen membrane. Symbols are colored with respect to the total adsorbed amount in the kerogen membranes according to the colormap shown in subfigure (a). Lines are guide for the eyes. (For interpretation of the references to color in this figure legend, the reader is referred to the web version of this article.)

pressures at the edges of the membranes. From the study of bulk fluids at equilibrium, we were able to establish correlations between partial pressures and fugacities (the reader is referred to the supplementary material for more details). Thus, we can evaluate the chemical potential gradients by applying these correlations to the pressure gradients calculated in situ during the simulations. Interestingly, mainly because

we maintain a homogeneous composition between the reservoirs, we observe a quasi linear relationship between the chemical potential gradients of CH₄ and CO₂ so that we may assume that $\nabla\mu_2 = \beta\nabla\mu_1$, where β is a temperature-dependent coefficient as reported in Table 2. This relation between the driving forces allows us to simplify the Eqs. (21) and (22) so as to show an affine relation between a flux J_i and the driving force $\nabla\mu_i$ applied to the corresponding species. This approach, as well as the calculation of the β coefficient discussed above, are described in detail in the supplementary material and allow us to deduce that the cross-correlation coefficient D_{12} is one to two orders of magnitude lower than the autocorrelation coefficients D_{11} and D_{22} . As a result, we neglected the inter-species cross-correlations to simplify the mass transport equations as

$$\frac{RTJ_i}{c\nabla\mu_i} = D_i y_i, \quad (23)$$

where we dropped one of the subscripts i in the notation of the collective diffusion coefficient to simplify the notations. As mentioned above, the collective diffusion coefficient D_i characterizes the displacement of the center of mass of the species i with respect to the rigid solid matrix. In the general case, it is decomposed into the contribution of the self-diffusion $D_{s,i}$ related to the individual displacements of the molecules, and a cross-correlation coefficient $D_{c,i}$ related to the correlated displacements between molecules of the same species :

$$D_i = D_{s,i} + D_{c,i} \quad (24)$$

Previous studies using molecular simulations, to which we contributed in part, have shown that the transport of hydrocarbon molecules in kerogen is dominated by self-diffusion (i.e. cross-correlation term, $D_{c,i}$, is negligible) [19–21]. As the self-diffusion coefficient decreases with fluid concentration, the collective diffusion coefficient was found to follow the same trend.

The solid lines in Fig. 9 show the fit of Eq. (23) to our simulation data and the values of the corresponding diffusion coefficients are reported in Table 4. In Fig. 9, because we investigated a range of chemical potentials gradients, several data points are plotted for each compositions of the adsorbed phase. Except for high CO₂ contents, the data points corresponding to given mixture compositions form clusters within data uncertainties. This demonstrates the linearity of the flux/force relationship in the transport equations and thus the independence of the diffusion coefficients from the $\nabla\mu_i$ driving forces. At a high content of CH₄, we see that the diffusion coefficient of the latter increases significantly since the points such as $y_1 \gtrsim 0.6$ are clearly above the fitted line. We attribute this behavior to the selective adsorption that favors CO₂ in the kerogen. Indeed, at high CH₄ content, CO₂ probably frees space in some percolating pathways, which should improve CH₄ diffusion. Such mechanisms therefore call into question the possibility of predicting the competitive diffusion of mixtures on the basis of diffusion coefficients obtained with pure species.

In spite of the rather large uncertainties we notice that fluid loading (represented by the coloring of data points) seems to slightly enhance the collective diffusion coefficients since the data corresponding to the highest fluid concentrations are very often found at the top of each cluster of data points. This effect is more noticeable for large amounts of CO₂, as the deviation from the line drawn by the fit of Eq. (23) appears to correlate fairly well with fluid loading. Although the uncertainty in the data does not allow a definitive conclusion to be drawn, this effect appears to be related to the emergence of cross-correlation diffusion mechanisms when the concentration of the adsorbed fluid increases. The mechanism becomes apparent at high fractions of CO₂ because, as the latter adsorbs better into the kerogen, it allows for higher fluid loadings.

At first reading, these results contradict previous findings regarding hydrocarbon diffusion in microporous kerogen models that show a decrease of the collective diffusion coefficient with fluid loading [19–21]. If the data from these studies were represented in the diagrams

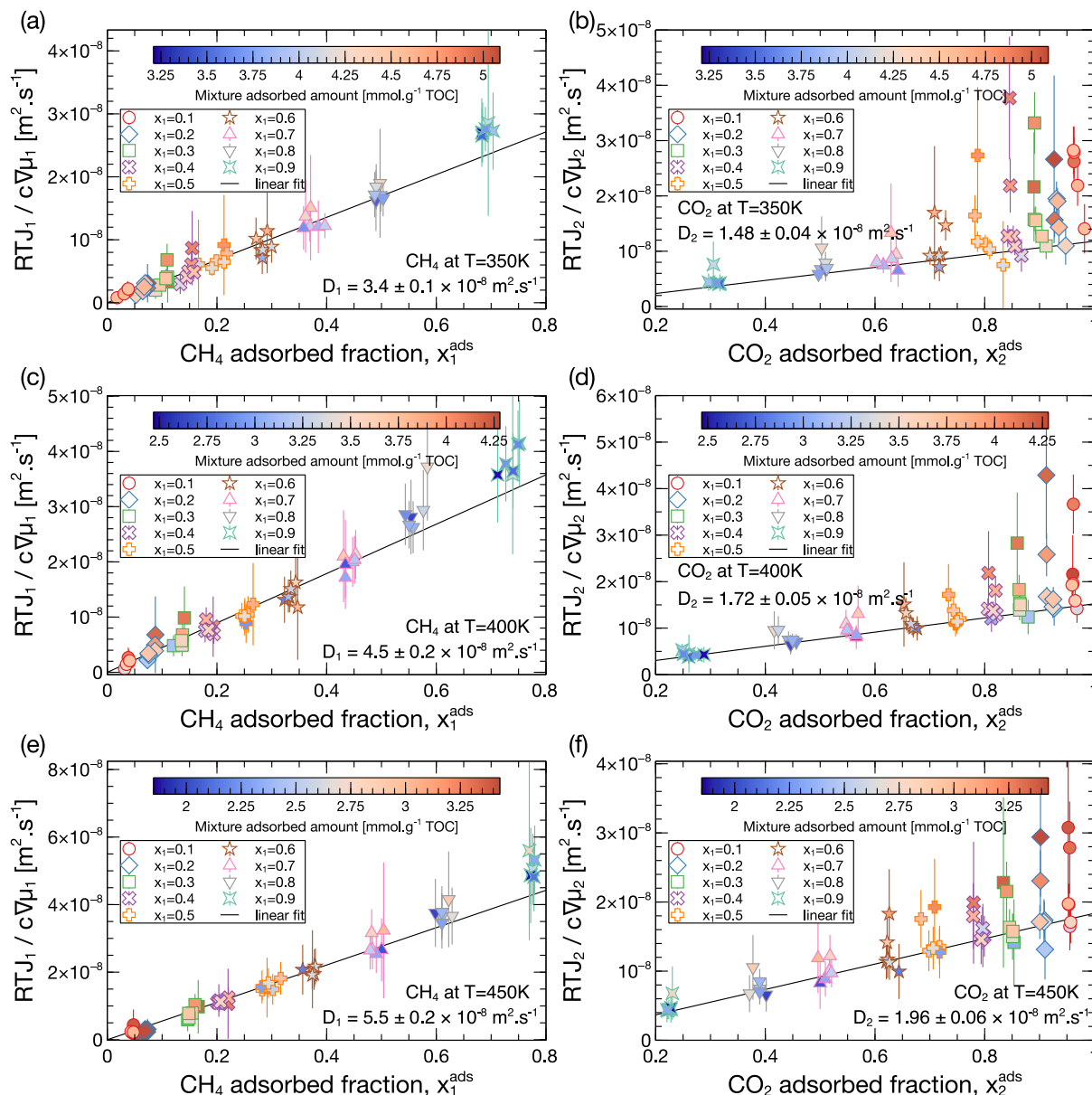


Fig. 9. Driving force acting on CO_2 , $\nabla\mu_2/RT$, plotted as a function of the driving force acting on CH_4 , $\nabla\mu_1/RT$. Results are shown for 350 K (a), 400 K (b), and 450 K (c). Different symbols stand for simulation data obtained for a range of CH_4 molar fraction in the bulk, x_1 . Symbols are colored with respect to the total adsorbed amount in the kerogen membranes according to the colormaps shown in each subfigure. (For interpretation of the references to color in this figure legend, the reader is referred to the web version of this article.)

of Fig. 9, for each composition we would observe points distributed vertically and of lower value the higher the fluid concentration. The difference with the results of the present study has several explanations. Firstly, our kerogen model includes a percolating pore with a diameter close to 1 nm (see Fig. 1) which can be sufficiently large to trigger correlated motion between fluid molecules when the concentration is high enough. This type of behavior has already been discussed by Boğan et al. who observed a collective diffusion coefficient that is almost independent of fluid loading due to the crossover between self and cross-correlated diffusion in the amorphous carbon model CS1000a [46]. Membrane models used in the work of Collell et al. [19], Falk et al. [20] and Obliger et al. [21] do not have such large percolating pores and should be more transposable to the expected behavior at the scale of kerogen nodules of several tens of nanometers, where the finite size effects observed in our study are unlikely or limited to the interface between micropores and mesopores. Secondly, the studies by Falk et al. and Obliger et al. involves only alkane molecules [20,21],

whereas in the study by Collell et al. only one fluid mixture contains CO_2 , and that in a very small proportion [19]. Therefore, these works did not study the transport of CO_2 -rich mixtures. The latter being a molecule with stronger interactions (both intra- and inter-species) than linear alkanes while being relatively mobile due to its small size, it is likely to enhance cross-correlated diffusion when present in large proportions in the microporous kerogen matrix. Since these pioneering works, many studies of fluid diffusion in kerogens based on molecular simulations have assumed that transport is dominated by self-diffusion and have dispensed with the calculation of the collective diffusion coefficient [22,26,51,69]. Nevertheless, we believe that for molecular models with sizes in the nanometer range, finite size effects such as those observed in our study may have been overlooked.

Regarding competitive diffusion, Table 4 also reports the ratio of the diffusion coefficients of CO_2 and CH_4 at the different temperatures studied. This ratio D_2/D_1 is in the range 0.36–0.43 and decreases slightly with the temperature varying from 350 K to 450 K. This ratio is

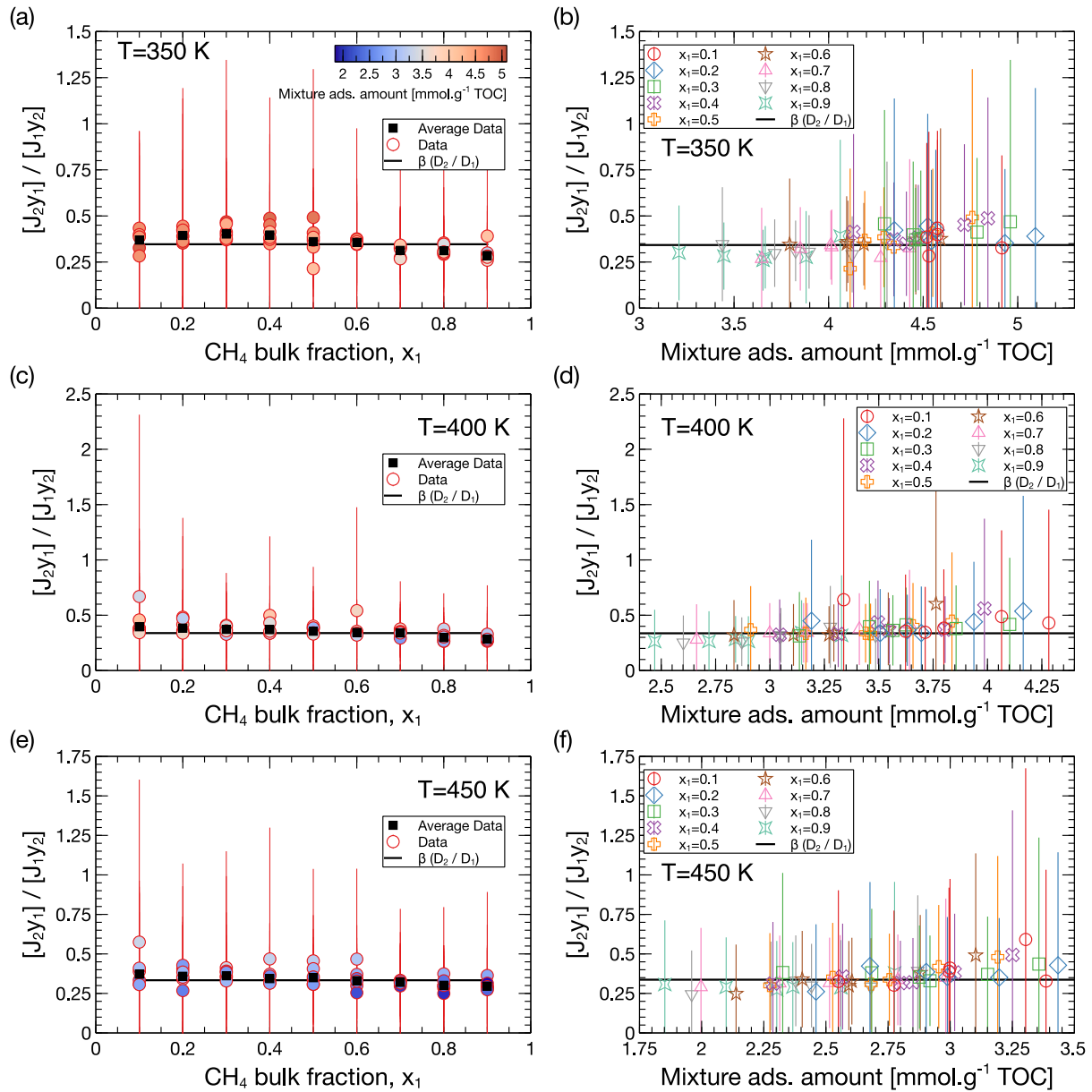


Fig. 10. Ratio $(J_2 y_1) / (J_1 y_2)$, plotted as a function of the molar fraction of CH_4 in the bulk (a, c, e) or as function of the fluid loading in the membrane (b, d, f). Results are shown for 350 K (a, b), 400 K (c, d), and 450 K (e, f). Circles stand for simulation data. In subfigures (a), (c) and (e) they are colored with respect to the total adsorbed amount in the kerogen membranes according to the colormap shown in subfigure (a), calibrated over the whole data set, regardless of temperature. Black squares stand for the weighted average of the data obtained at each value of x_1 , with weights set proportional to the inverse of the data uncertainties. The solid lines stand for the quantity $\beta(D_2/D_1)$. (For interpretation of the references to color in this figure legend, the reader is referred to the web version of this article.)

significantly lower than that obtained by other authors (~ 0.6 – 0.9), for the self-diffusion of CO_2/CH_4 mixtures in a type-II kerogen molecular model [22,26]. This discrepancy can be explained by the consideration of cross-correlation mechanisms in the estimation of diffusion coefficients in our study. It is also possible that our method employing a finite size kerogen membrane introduces a flow resistance effect at the interface between the solid matrix and the bulk reservoir, as documented in the work of Liu et al. [70]. In the case of an amorphous carbon molecular model, they found that interfacial resistance could reduce the collective diffusion coefficient of CH_4 by a factor 2. CO_2 would be even more affected by these surface effects due to selective adsorption and would have its diffusion coefficient reduced accordingly. By considering Eq. (23) valid for our data set, we can deduce

the following relation:

$$\frac{J_2 y_1}{J_1 y_2} = \frac{\nabla \mu_2 D_2}{\nabla \mu_1 D_1} = \beta \frac{D_2}{D_1} \quad (25)$$

where we used $\nabla \mu_2 = \beta \nabla \mu_1$. In Fig. 10, by plotting the quantity $J_2 y_1 / J_1 y_2$ we can therefore investigate the effects of mixture composition and fluid loading on the ratio of species diffusion coefficients. Despite the obvious effect of cross-correlated diffusion on mass transport discussed in the previous paragraph, our results suggest that this does not significantly impact the competitive diffusion between CO_2 and CH_4 , as evidenced by the results plotted in Fig. 10. Indeed, although the data points suggest that fluid concentration causes a slight increase in the D_2/D_1 ratio, this effect can be neglected to a good approximation. On the other hand, as expected, we do observe a slight effect of the mixture composition on our results, as the diffusion of CH_4 is enhanced when it dominates the mixture. Thus, for a methane

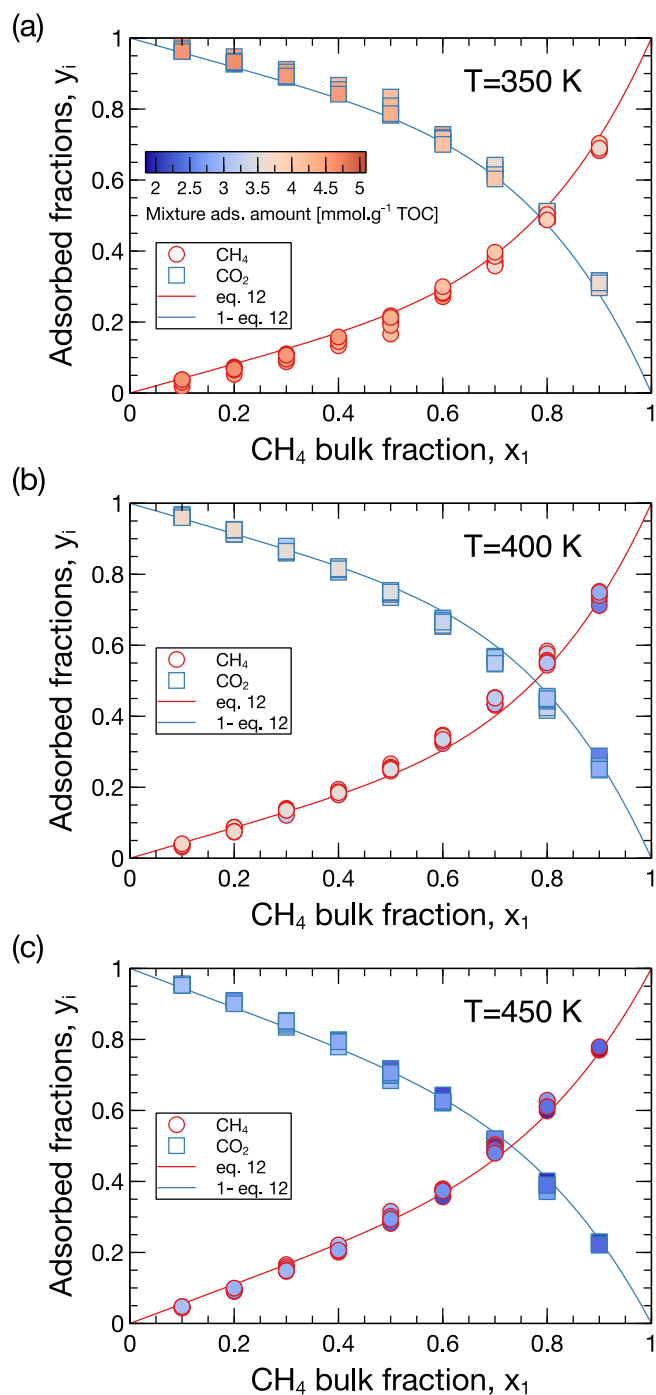


Fig. 11. Mole fractions in the adsorbed phase, y_i , plotted as a function of CH_4 bulk mole fraction, x_1 , obtained under non equilibrium conditions at 350 K (a), 400 K (b), and 450 K (c). Circles and squares symbols stand for simulation data obtained for CH_4 and CO_2 , respectively. All symbols are colored with respect to the total adsorbed amount in the kerogen membranes according to the colormap shown in subfigure (a), calibrated over the whole data set, regardless of temperature. The red solid line and blue solid line stand for the prediction of the CEL model with the same parameters as those fitted to equilibrium simulations data. (For interpretation of the references to color in this figure legend, the reader is referred to the web version of this article.)

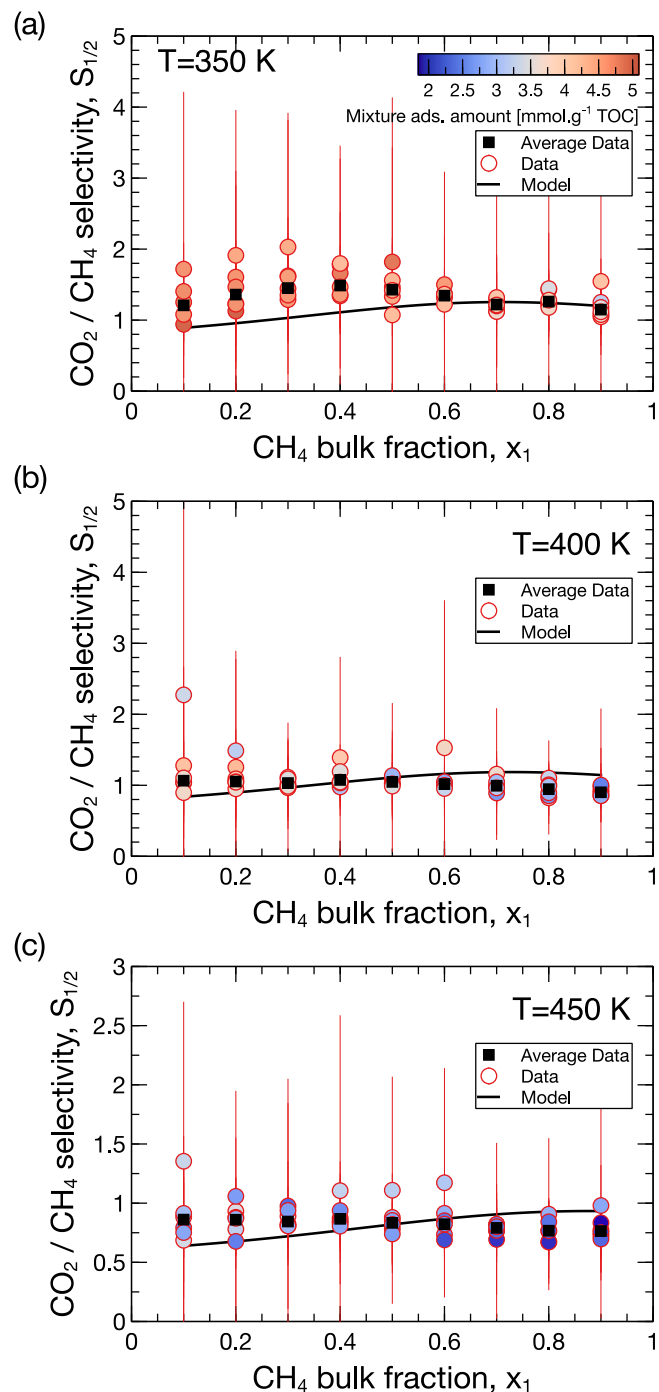


Fig. 12. CO_2/CH_4 selectivity due to transport and adsorption, plotted as a function of CH_4 bulk mole fraction, x_1 , at 350 K (a), 400 K (b), and 450 K (c). Circles stand for simulation data. Symbols are colored with respect to the total adsorbed amount in the kerogen membranes according to the colormap shown in subfigure (a), calibrated over the whole data set, regardless of temperature. Black squares stand for the weighted average of the data obtained at each value of x_1 , with weights set proportional to the inverse of the data uncertainties. The red solid lines stand for the predictions of Eq. (26). (For interpretation of the references to color in this figure legend, the reader is referred to the web version of this article.)

Table 4

Diffusion coefficients from the fit of Eq. (23) to our simulation data.

Species	D_i [10^{-8} m ² s ⁻¹]		
	350 K	400 K	450 K
CH ₄	3.4 ± 0.1	4.5 ± 0.2	5.5 ± 0.2
CO ₂	1.48 ± 0.04	1.72 ± 0.05	1.96 ± 0.06
Ratio	D_2/D_1		
	350 K	400 K	450 K
CO ₂ /CH ₄	0.43 ± 0.02	0.38 ± 0.03	0.36 ± 0.02

composition ranging from 10% to 90%, the ratio of diffusion coefficients decreases from 0.46 to 0.37, 0.44 to 0.32 and 0.40 to 0.32 for temperatures of 350 K, 400 K and 450 K, respectively. Although this effect is undeniable, it remains of limited magnitude, introducing variations of the order of $\pm 15\%$ compared to the values reported in Table 4. To a fair approximation, we can thus conclude that the ratio of the diffusion coefficients, deduced from the fit of Eq. (23) to our data, is representative of the competitive transport of the mixtures CO₂/CH₄ in the studied kerogen model.

More generally, the separation of mixtures in a microporous membrane such as kerogen results from the combination of selective diffusion, discussed previously, and selective adsorption under non-equilibrium conditions. We have studied in detail the selective adsorption of CH₄/CO₂ mixtures under equilibrium conditions in the previous section. As already mentioned, in order to isolate the effect of flow on selective adsorption, we imposed pressure gradients while maintaining homogeneous mixture compositions between the upstream and downstream bulk reservoirs during our non-equilibrium simulations to allow comparison with our equilibrium results. Fig. 11 shows the comparison between the compositions of the adsorbed phases observed in the non-equilibrium simulations and the CEL model predictions generated with the α and γ parameters obtained from the equilibrium data analysis. The agreement between the compositions of the adsorbed mixtures at equilibrium and non-equilibrium is excellent. These results demonstrate that the CEL adsorption model proposed in this study can be used to predict the selective non-equilibrium adsorption of CH₄/CO₂ mixtures in kerogen. For further evidence of this assertion, the interested reader is referred to a detailed analysis of the influence of pressure on the adsorbed quantities under non-equilibrium conditions, available in supplementary material. The overall selectivity, denoted $S_{2/1}$ taking into account both adsorption and diffusion in the membrane, is then defined as:

$$S_{2/1} = \frac{J_2}{J_1} \times \frac{x_1}{x_2}. \quad (26)$$

Since in the particular case of our study, $\nabla \mu_2 = \beta \nabla \mu_1$, we can rewrite the selectivity as follows:

$$S_{2/1} = \left(\frac{\nabla \mu_2 D_2}{\nabla \mu_1 D_1} \right) S_{2/1}^{ads} = \beta \left(\frac{D_2}{D_1} \right) S_{2/1}^{ads} \quad (27)$$

where we used Eqs. (8) and (23) in combination with (26). In Fig. 12, we plot the overall selectivities obtained by applying Eq. (26) to our non-equilibrium simulation data. Comparing with the data presented in Fig. 5, we immediately observe that the overall selectivity is significantly lower than the selectivity due to adsorption alone. Again the large uncertainties do not allow a definitive conclusion, but the overall selectivity is of the order of 1. If it seems rather in favor of CO₂ at 350 K, according to our results the selectivity probably reverses in favor of CH₄ when the temperature increases above 400 K. On these graphs we have also plotted, in solid lines, the predictions generated by the formula proposed in Eq. (27). To do this, we used the β values reported in Table 2, and we used the ratios of the diffusion coefficients reported in Table 4. As for the selectivity due to adsorption, $S_{2/1}^{ads}$, we used the CEL model prediction given by Eq. (14) with parameters deduced from the equilibrium data. Although it is difficult to judge the adequacy

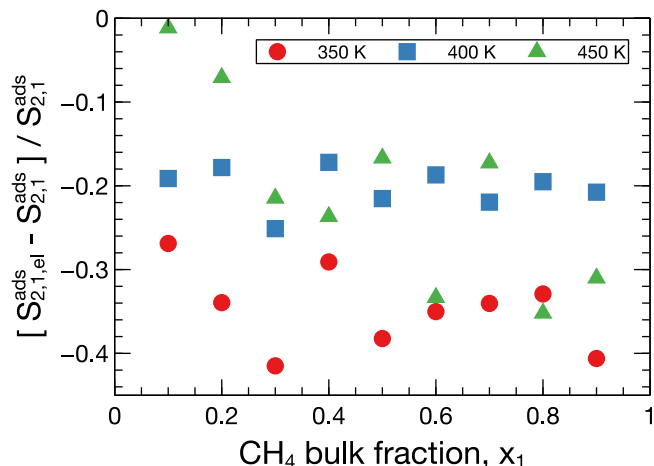


Fig. A.13. Evolution of the relative error on the adsorption selectivity as predicted by the EL model as a function of the molar fraction of CH₄ in the bulk.

between the data and this prediction with respect to the evolution with the composition of the mixture, we observe that the prediction tends to underestimate the selectivity at low levels of CH₄ and to overestimate it at high levels. This trend follows exactly that observed for the ratio of diffusion coefficients discussed earlier. Nonetheless, the order of magnitude of the selectivity as well as its decrease with temperature is captured correctly. We can therefore conclude that the simple formalism of Eq. (27) could be used to quantify the selectivity of kerogen towards flowing CH₄/CO₂ gas mixtures.

5. Conclusion and perspectives

In this study, we have chosen to study the adsorption and competitive diffusion of CH₄/CO₂ mixtures through a molecular model of mature type-II kerogen in the manner of a numerical experiment. Indeed, we used the DCV-GCMD method to put the kerogen membrane in contact with bulk reservoirs whose pressure and composition were controlled. In this way, we used an identical system and the same methodology to explore both equilibrium adsorption and membrane separation under a pressure gradient. We have analyzed our results focusing on the selectivity of kerogen towards mixtures for a wide range of thermodynamic conditions.

Under equilibrium conditions in our system, the adsorption selectivity of CO₂/CH₄ is roughly in the range of 2–4 and was found to decrease with temperature in the range 350–450 K. We compared our results to the predictions of classical adsorption models, such as the Extended Langmuir (EL) model and the Loading Ratio Correlation (LRC) model. We were able to quickly discard the latter since it predicts diverging selectivities for asymmetric binary mixture compositions. On the other hand, the EL model tends to underestimate the selectivity in a systematic way and can be considered as a lower bound. In order to improve the prediction of the adsorption of CH₄/CO₂ mixtures in kerogen, we proposed a correction of the EL model by representing the composition of the adsorbed phase by a Redlich–Kister polynomial. With the objective of offering a simple approach to petroleum engineers, we constrained the correlation so that only one adjustable parameter is needed to significantly improve the predictions on the adsorption isotherms. This new empirical model, named Corrected Extended Langmuir (CEL), like the EL model, generates an adsorption selectivity independent of the pressure but which can vary with the composition of the mixture. The additional adjustable parameter takes the form of an exponent denoted γ which, in our study, appears to be weakly dependent on thermodynamic conditions. Thus, we find that a value of $\gamma = 4.9 \pm 0.3$ can be used to obtain satisfactory results

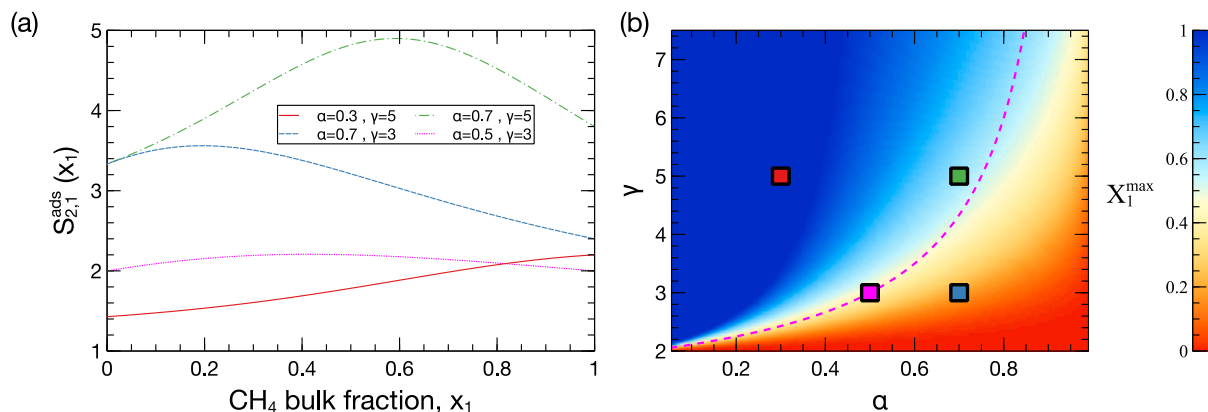


Fig. A.14. (a) Adsorption selectivity as a function of the molar fraction of CH_4 in the bulk, computed for a set of model parameters (α, γ) . (b) Molar fraction of CH_4 in the bulk that maximizes adsorption selectivity in the parameters phase space (α, γ) . The magenta dotted line stands for the subset of parameters providing equal selectivities at $x_1 = 0$ and $x_1 = 1$. Colored squares correspond to the set of parameters used to compute the selectivities in subfigure (a). (For interpretation of the references to color in this figure legend, the reader is referred to the web version of this article.)

for all the conditions explored in our study. It will be interesting in a future work to investigate other molecular models of kerogen, or, more generally, other amorphous carbons, to verify how this parameter depends on the studied systems. One possible approach would be to look for topological (pore size, specific surface area, aromaticity, etc.) or chemical (chemical functional groups, proportion of heteroatoms) descriptors that would influence the γ value for a collection of kerogen molecular models. In addition, the adsorption-induced swelling mechanism should be taken into account in the case of molecular models supposed to represent more flexible materials than the one studied here.

Out of equilibrium, we observed that the adsorption selectivity is not affected by the flow conditions when a pressure gradient is imposed across the kerogen membrane. Therefore, the CEL model can be used to describe the contribution of adsorption to the selectivity of kerogen under flow conditions. In the manner of an experiment, we were able to calculate gas permeabilities for a variety of driving force magnitudes (pressure gradient), fluid loading (average pressure), mixture composition and temperatures. We observe a crossing of the partial permeabilities of the two species for a molar fraction of bulk methane between 0.4 and 0.6. To decouple the contributions of fluid loading and diffusivity, we inferred the value of the collective diffusion coefficients of CH_4 and CO_2 from our raw data. We found that the inter-species correlation could be neglected and that to a good approximation each species responded only to the driving force directly applied to it. In contrast, probably due to finite size and interfacial effects present in our system, the collective diffusion coefficients increase with fluid loading suggesting the occurrence of cross-correlation diffusion often overlooked in other works on similar systems. These results will nevertheless require further work to identify precisely what causes these mechanisms to appear in our system. From the point of view of competitive CO_2/CH_4 diffusion, we found a ratio of the collective diffusion coefficients of the order of 0.3–0.4, which is about two times lower than the results of other simulations found in the literature, neglecting the cross-correlation diffusion effects discussed earlier. This ratio decreases with temperature and depends rather weakly on the fluid concentration and the composition of the mixture in the studied range.

To describe the global selectivity of our kerogen model, which combines the effect of adsorption and diffusion, we propose a simple approach summarized by Eq. (27) where we jointly use the proposed CEL model and the average ratio of diffusion coefficients deduced from simulations. With our method, the overall selectivity of our kerogen model that combines the effect of adsorption and diffusion is therefore of the order of ~ 1 . If CO_2 wins the competition at low temperatures, this selectivity is reversed around 400 K. Although it will be necessary to verify the validity of these orders of magnitude by elucidating the

impact of finite size effects on the value of the obtained diffusion coefficients, our approach reproduces the global selectivity correctly. We believe that this simple formal framework can be incorporated into larger scale models, including reservoir simulations, to better account for kerogen selectivity towards CH_4/CO_2 mixtures in the context of enhanced natural gas recovery in shales. The extension of our approach to other molecular models of kerogen, including the effect of moisture content, possible coupling to solid matrix deformation [56] or the impact of mesopores on flow mechanisms [71,72], is left for future work.

CRediT authorship contribution statement

Patrick A. Bonnaud: Investigation, Methodology, Writing – original draft, Writing – review & editing, Formal analysis. **Fouad Oulebsir:** Methodology. **Guillaume Galliero:** Funding acquisition, Investigation, Validation, Writing – review & editing. **Romain Vermorel:** Formal analysis, Funding acquisition, Investigation, Methodology, Supervision, Validation, Writing – original draft, Writing – review & editing.

Declaration of competing interest

The authors declare that they have no known competing financial interests or personal relationships that could have appeared to influence the work reported in this paper.

Data availability

Data will be made available on request

Acknowledgments

The authors gratefully acknowledge TotalEnergies for providing financial support as well as computational resources for the fulfillment of this project. The authors also acknowledge Université de Pau et des Pays de l'Adour (UPPA) and Mésocentre de Calcul Intensif Aquitain (MCIA) for providing additional computational resources.

Appendix A. Details on the Corrected Extended Langmuir model

Here we discuss in more details the predictions of the CEL model as a function of the values assigned to the parameters α and γ , as they appear in the expression for the selectivity $S_{2,1}^{ads}$ given by Eq. (14). The selectivity appears there as a function of the bulk composition of the binary mixture through the variable x_1 on the interval $[0; 1]$. If the computation of $S_{2,1}^{ads}(x_1 \rightarrow 0) = 1/(1 - \alpha)$ is trivial, the limit of the

function when $x_1 \rightarrow 1$ requires to rework the expression of Eq. (14) to eliminate the singularity in the denominator. The first step is to reshape the numerator as follows:

$$S_{2/1}^{\text{ads}} = \frac{1 - x_1 + \alpha x_1(1 - x_1^{\gamma-1})}{(1 - x_1)(1 - \alpha + \alpha x_1^{\gamma-1})}. \quad (\text{A.1})$$

Since $\gamma \geq 2$, as discussed in the body of the article, we can use the remarkable identity $1 - x_1^{\gamma-1} = (1 - x_1)(x_1^{\gamma-2} + x_1^{\gamma-3} + \dots + x_1 + 1)$ to obtain

$$S_{2/1}^{\text{ads}} = \frac{1 + \alpha x_1(x_1^{\gamma-2} + x_1^{\gamma-3} + \dots + x_1 + 1)}{1 - \alpha + \alpha x_1^{\gamma-1}}, \quad (\text{A.2})$$

which indeed removed the singularity at $x_1 = 1$. The selectivity at $x_1 = 1$ is then easily calculated to obtain $S_{2/1}^{\text{ads}}(x_1 \rightarrow 1) = 1 + \alpha(\gamma - 1)$. For $0 \leq \alpha \leq 1$ and $\gamma \geq 2$, the numerical study of the function S on the interval $x_1 \in [0; 1]$ shows that the latter either increases monotonically or passes through a maximum. The Fig. A.14 shows how the choice of the parameters γ and α affects the shape of the curve as well as the value of x_1 at which the maximum selectivity is observed. Please note that we have not studied other possible values for the parameters α and γ because the objective is to keep the typical bell-shaped appearance of the parity plots shown in Fig. 4, as discussed in the body of the paper. Although using the two parameters of the correlation as independent degrees of freedom would undoubtedly allow a finer adjustment of our simulation results, we wanted to propose a simple approach to improve the prediction of competitive adsorption of mixtures by relying as much as possible on the adsorption data of pure species. To do so, we imposed that the selectivities of the classical EL model be found at $x_1 \rightarrow 0$, which corresponds to the case where the CO_2 dominates the mixture. Indeed, although the effect is not very strong, our results, as shown in Fig. A.13, suggest that the difference between the simulated selectivity and that given by the EL model is smaller when $x_1 \rightarrow 0$.

Appendix B. Supplementary data

Supplementary material related to this article can be found online at <https://doi.org/10.1016/j.fuel.2023.129020>.

References

- [1] Wang Q, Li R. Research status of shale gas: A review. *Renew Sustain Energy Rev* 2017;74:715–20. <http://dx.doi.org/10.1016/j.rser.2017.03.007>, URL <https://www.sciencedirect.com/science/article/pii/S1364032117303210>.
- [2] Inventory of U.S. greenhouse gas emissions and sinks: 1990–2020. 2022, [online].
- [3] Omari A, Wang C, Li Y, Xu X. The progress of enhanced gas recovery (EGR) in shale gas reservoirs: A review of theory, experiments, and simulations. *J Pet Sci Eng* 2022;213(110461).
- [4] Vandenbroucke M. Kerogen: from types to models of chemical structure. *Oil Gas Sci Technol - Rev IFP* 2003;58(2):243–269.
- [5] Vandenbroucke M, Largeau C. Kerogen origin, evolution and structure. *Org Geochem* 2007;38:719–833.
- [6] Ross DJK, Bustin RM. The importance of shale composition and pore structure upon gas storage potential of shale gas reservoirs. *Mar Pet Geol* 2009;26:916–27.
- [7] Heller R, Zoback M. Adsorption of methane and carbon dioxide on gas shale and pure mineral samples. *J Unconv Oil Gas Resour* 2014;8:14–24.
- [8] Gasparik M, Bertier P, Gensterblum Y, Ghanizadeh A, Krooss BM, Littke R. Geological controls on the methane storage capacity in organic-rich shales. *Int J Coal Geol* 2014;123:34–51.
- [9] Huang L, Ning Z, Wang Q, Zhang W, Cheng Z, Wu X, Qin H. Effect of organic type and moisture on CO_2/CH_4 competitive adsorption in kerogen with implications for CO_2 sequestration and enhanced CH_4 recovery. *Appl Energy* 2018;210:28–43.
- [10] Gasparik M, Ghanizadeh A, Bertier P, Gensterblum Y, Bouw S, Krooss BM. High-pressure methane sorption isotherms of black shales from The Netherlands. *Energy Fuels* 2012;26:4995–5004.
- [11] Rexer TFF, Benhem MJ, Aplin AC, Thomas KM. Methane adsorption on shale under simulated geological temperature and pressure conditions. *Energy Fuels* 2013;27:3099–109.
- [12] Ortiz Cancino OP, Pérez DP, Pozo M, Bessieres D. Adsorption of pure CO_2 and a CO_2/CH_4 mixture on a black shale sample: Manometry and microcalorimetry measurements. *J Pet Sci Eng* 2017;159:307–13.
- [13] Li J, Zhou S, Gaus G, Li Y, Ma Y, Chen K, Zhang Y. Characterization of methane adsorption on shale and isolated kerogen from the Sichuan Basin under pressure up to 60 MPa: Experimental results and geological implications. *Int J Coal Geol* 2018;189:83–93.
- [14] Obliger A, Bousige C, Coasne B, Leyssale J-M. Development of atomistic kerogen models and their applications for gas adsorption and diffusion: A mini-review. *Energy Fuels* 2023. <http://dx.doi.org/10.1021/acs.energyfuels.2c03633>.
- [15] Collett J, Galliero G, Gouth F, Montel F, Pujol M, Ungerer P, Yiannourakou M. Molecular simulation and modelisation of methane/ethane mixtures adsorption onto a microporous molecular model of kerogen under typical reservoir conditions. *Microporous Mesop Mater* 2014;197:194–203. <http://dx.doi.org/10.1016/j.micromeso.2014.06.016>, URL <https://www.sciencedirect.com/science/article/pii/S1387181114003345>.
- [16] Falk K, Pellenq RJ-M, Ulm F-J, Coasne B. Effect of chain length and pore accessibility on alkane adsorption in kerogen. *Energy Fuels* 2015;29(12):7889–96.
- [17] Bousige C, Ghimbeu CM, Vix-Guterl C, Pomerantz AE, Suleimenova A, Vaughan G, Garbarino G, Feynson M, Wildgruber C, Ulm F-J, Pellenq RJ-M, Coasne B. Realistic molecular model of kerogen's nanostructure. *Nature Mater* 2016;15:576–82.
- [18] Afagwu C, Al-Afnan S, Patil S, Aljaberi J, Mahmoud MA, Li J. The impact of pore structure and adsorption behavior on kerogen tortuosity. *Fuel* 2021;303:121261. <http://dx.doi.org/10.1016/j.fuel.2021.121261>, URL <https://www.sciencedirect.com/science/article/pii/S0016236121011406>.
- [19] Collett J, Galliero G, Vermorel R, Ungerer P, Yiannourakou M, Montel F, Pujol M. Transport of multicomponent hydrocarbon mixtures in shale organic matter by molecular simulations. *J Phys Chem C* 2015;119:22587–22595. <http://dx.doi.org/10.1021/acs.jpcc.5b07242>.
- [20] Falk K, Coasne B, Pellenq RJ-M, Ulm F-J, Bocquet L. Subcontinuum mass transport of condensed hydrocarbons in nanoporous media. *Nature Commun* 2015;6:6949.
- [21] Obliger A, Pellenq RJ-M, Ulm F-J, Coasne B. Free volume theory of hydrocarbon mixture transport in nanoporous materials. *J Phys Chem Lett* 2016;7:3712–7.
- [22] Wang Z, Li Y, Liu H, Zeng F, Guo P, Jiang W. Study on the adsorption, diffusion and permeation selectivity of shale gas in organics. *Energies* 2017;10(142).
- [23] Pathak M, Huang H, Meakin P, Deo M. Molecular investigation of the interactions of carbon dioxide and methane with kerogen: Application in enhanced shale gas recovery. *J Nat Gas Sci Eng* 2018;51:1–8.
- [24] Wang T, Tian S, Li G, Sheng M, Ren W, Liu Q. Molecular simulation of CO_2/CH_4 competitive adsorption on shale kerogen for CO_2 sequestration and enhanced gas recovery. *J Phys Chem C* 2018;122:17009–18.
- [25] Wang T, Tian S, Li G, Sheng M. Selective adsorption of supercritical carbon dioxide and methane binary mixture in shale kerogen nanopores. *J Nat Gas Sci Eng* 2018;50:181–8.
- [26] Sui H, Zhang F, Wang Z, Wang D, Wang Y. Effect of kerogen maturity, water content for carbon dioxide, methane, and their mixture adsorption and diffusion in kerogen: A computational investigation. *Langmuir* 2020;36(33):9756–69. <http://dx.doi.org/10.1021/acs.langmuir.0c01191>, arXiv:<https://doi.org/10.1021/acs.langmuir.0c01191>, PMID: 32787125.
- [27] Alafnan S, Falola Y, Al Mansour O, AlSamadony K, Awotunde A, Aljawad M. Enhanced recovery from organic-rich shales through carbon dioxide injection: Molecular-level investigation. *Energy Fuels* 2020;34(12):16089–98. <http://dx.doi.org/10.1021/acs.energyfuels.0c03126>, arXiv:<https://doi.org/10.1021/acs.energyfuels.0c03126>.
- [28] Sun Z, Li Y, Lu L, Zhu J, Yang Z, Qu J, Xue H, Ouyang J. Molecular simulation of CH_4 nanoscale behavior and enhanced gas recovery in organic-rich shale. *Geofluids* 2022;2022:2420869. <http://dx.doi.org/10.1155/2022/2420869>.
- [29] Huang L, Ning Z, Wang Q, Qi R, Zeng Y, Qin H, Ye H, Zhang W. Molecular simulation of adsorption behaviors of methane, carbon dioxide and their mixtures on kerogen: Effect of kerogen maturity and moisture content. *Fuel* 2018;211:159–72.
- [30] Li J, Wang Y, Chen Z, Rahman SS. Insights into the molecular competitive adsorption mechanism of CH_4/CO_2 in a kerogen matrix in the presence of moisture, salinity, and ethane. *Langmuir* 2021;37(43):12732–45. <http://dx.doi.org/10.1021/acs.langmuir.1c02274>, arXiv:<https://doi.org/10.1021/acs.langmuir.1c02274>, PMID: 34668376.
- [31] Ungerer P, Collett J, Yiannourakou M. Molecular modeling of the volumetric and thermodynamic properties of kerogen: Influence of organic type and maturity. *Energy Fuels* 2015;29:91–105.
- [32] Collett J, Ungerer P, Galliero G, Yiannourakou M, Montel F, Pujol M. Molecular simulation of bulk organic matter in type II shales in the middle of the oil formation window. *Energy Fuels* 2014;28:7457–66.
- [33] Plimpton S. Fast parallel algorithms for short-range molecular dynamics. *J Comput Phys* 1995;117:1–19.
- [34] Sun H. COMPASS: An ab initio force-field optimized for condensed-phase applications - overview with details on alkane and benzene compounds. *J Phys Chem B* 1998;102(38):7338–64.
- [35] Nosé S. A unified formulation of the constant temperature molecular dynamics methods. *J Chem Phys* 1984;81:511–9.
- [36] Hoover WG. Canonical dynamics: Equilibrium phase-space distributions. *Phys Rev A* 1985;31:1695–7.

- [37] Parrinello M, Rahman A. Polymorphic transitions in single crystals: A new molecular dynamics method. *J Appl Phys* 1981;52(12):7182–90.
- [38] Deserno M, Holm C. How to mesh up Ewald sums. I. A theoretical and numerical comparison of various particle mesh routines. *J Chem Phys* 1998;109:7678–93.
- [39] Oulebsir F. Transport de fluides dans les matériaux microporeux (Ph.D. thesis), Université de Pau et des Pays de l'Adour, Laboratoire des Fluides Complexes et leurs Réservoirs, UMR 5150 CNRS-TOTAL-UPPA; 2017.
- [40] Herrera L, Do DD, Nicholson D. A Monte Carlo integration method to determine accessible volume, accessible surface area and its fractal dimension. *J Colloid Interface Sci* 2010;348:529–36.
- [41] Bhattacharya S, Gubbins KE. Fast method for computing pore size distributions of model materials. *Langmuir* 2006;22(18):7726–31.
- [42] MacElroy JMD. Nonequilibrium molecular dynamics simulation of diffusion and flow in thin microporous membranes. *J Chem Phys* 1994;101(6):5274–80.
- [43] Heffelfinger GS, van Swol F. Diffusion in Lennard-Jones fluids using dual control volume grand canonical molecular dynamics simulation (DCV-GCMD). *J Chem Phys* 1994;100(10):7548–52.
- [44] Cracknell RF, Nicholson D, Quirke N. Direct molecular dynamics simulation of flow down a chemical potential gradient in a slit-shaped micropore. *Phys Rev Lett* 1995;74(13):2463–6.
- [45] Vieira-Linhares AM, Seaton NA. Non-equilibrium molecular dynamics simulation of gas separation in a microporous carbon membrane. *Chem Eng Sci* 2003;58:4129–36.
- [46] Bojan A, Vermorel R, Ulm F-J, Pellenq RJ-M. Molecular simulations of supercritical fluid permeation through disordered microporous carbons. *Langmuir* 2013;29(32):9985–90. <http://dx.doi.org/10.1021/la402087r>.
- [47] Brochard L, Vandamme M, Pellenq RJ-M, Fen-Chong T. Adsorption-induced deformation of microporous materials: Coal swelling induced by CO_2 - CH_4 competitive adsorption. *Langmuir* 2012;28:2659–70.
- [48] Ho TA, Criscenti LJ, Wang Y. Nanostructural control of methane release in kerogen and its implications to wellbore production decline. *Sci Rep* 2016;6:28053.
- [49] Kazemi M, Maleki H, Takbiri-Borujeni A. Molecular dynamics study of transport and storage of methane in kerogen. *Society of Petroleum Engineer*; 2016, SPE-184058-MS.
- [50] Vasileiadis M, Peristeras LD, Papavasileiou KD, Economou IG. Modeling of bulk kerogen porosity: Methods for control and characterization. *Energy Fuels* 2017;31:6004–18.
- [51] Vasileiadis M, Peristeras LD, Papavasileiou KD, Economou IG. Transport properties of shale gas in relation to kerogen porosity. *J Phys Chem C* 2018;122(11):6166–77.
- [52] Wu T, Firoozabadi A. Methane flow in shale nanopores with kerogen microstructure by molecular dynamics. *Society of Petroleum Engineers*; 2018, SPE-191686-MS.
- [53] Feng F, Akkutlu IY. A simple molecular kerogen pore-network model for transport simulation in condensed phase digital source-rock physics. *Transp Porous Media* 2019;126(2):295–315.
- [54] Kazemi M, Takbiri-Borujeni A. Flow of gases in organic nanocapillary pores of shale: A boundary-driven molecular simulation study. *Society of Petroleum Engineers*; 2016, SPE-180441.
- [55] Arya G, Chang H-C, Maginn EJ. A critical comparison of equilibrium, non-equilibrium and boundary-driven molecular dynamics techniques for studying transport in microporous materials. *J Chem Phys* 2001;115(17):8112–24. <http://dx.doi.org/10.1063/1.1407002>, arXiv:https://doi.org/10.1063/1.1407002.
- [56] Ariskina K, Galliero G, Obliger A. Free volume model for transport in flexible kerogen of source rock's organic matter. *J Phys Chem B* 2022;126(38):7409–17. <http://dx.doi.org/10.1021/acs.jpcc.2c03970>, URL <https://hal.archives-ouvertes.fr/hal-03893019>.
- [57] Frenkel D, Smit B. Understanding molecular simulation: From algorithms to applications. 2nd ed.. London: Academic Press; 2002.
- [58] Efron B, Tibshirani R. Bootstrap methods for standard errors, confidence intervals, and other measures of statistical accuracy. *Statist Sci* 1986;1(1):54–75. <http://dx.doi.org/10.1214/ss/1177013815>.
- [59] Langmuir I. The adsorption of gases on plane surfaces of glass, mica and platinum. *J Am Chem Soc* 1918;40(9):1361–403. <http://dx.doi.org/10.1021/ja02242a004>.
- [60] Kapoor A, Ritter JA, Yang RT. An extended langmuir model for adsorption of gas mixtures on heterogeneous surfaces. *Langmuir* 1990;6(3):660–4.
- [61] Brunauer S, Emmett PH, Teller E. Adsorption of gases in multimolecular layers. *J Am Chem Soc* 1938;60(2):309–19.
- [62] Duan S, Gu M, Du X, Xian X. Adsorption equilibrium of CO_2 and CH_4 and their mixture on sichuan basin shale. *Energy Fuels* 2016;30:2248–56.
- [63] Khosrowshahi MS, Abdol MA, Mashhadimoslem H, Khakpour E, Emrooz HBM, Sadeghzadeh S, Ghaemi A. The role of surface chemistry on CO_2 adsorption in biomass-derived porous carbons by experimental results and molecular dynamics simulations. *Sci Rep* 2022;12(1):8917. <http://dx.doi.org/10.1038/s41598-022-12596-5>.
- [64] Liu L, Nicholson D, Bhatia SK. Adsorption of CH_4 and CH_4/CO_2 mixtures in carbon nanotubes and disordered carbons: A molecular simulation study. *Chem Eng Sci* 2015;121:268–78. <http://dx.doi.org/10.1016/j.ces.2014.07.041>, URL <https://www.sciencedirect.com/science/article/pii/S0009250914003868>, 2013 Danckwerts Special Issue on Molecular Modelling in Chemical Engineering.
- [65] Glatz G, Alafnan S, Raza A, Mahmoud M. Multicomponent gas adsorption behavior of kerogen: A molecular investigation. *Energy Fuels* 2022;36(13):6695–710. <http://dx.doi.org/10.1021/acs.energyfuels.2c01469>, arXiv:https://doi.org/10.1021/acs.energyfuels.2c01469.
- [66] Krishna R. Elucidation and characterization of entropy effects in mixture separations with micro-porous crystalline adsorbents. *Sep Purif Technol* 2019;215:227–41. <http://dx.doi.org/10.1016/j.seppur.2019.01.014>, URL <https://www.sciencedirect.com/science/article/pii/S1383586618328478>.
- [67] Van Assche TRC, Baron GV, Denayer JFM. An explicit multicomponent adsorption isotherm model: accounting for the size-effect for components with langmuir adsorption behavior. *Adsorption* 2018;24(6):517–30. <http://dx.doi.org/10.1007/s10450-018-9962-1>.
- [68] Redlich O, Kister AT. Algebraic representation of thermodynamic properties and the classification of solutions. *Ind Eng Chem* 1948;40(2):345–8. <http://dx.doi.org/10.1021/ie50458a036>.
- [69] Sui H, Yao J. Effect of surface chemistry for CH_4/CO_2 adsorption in kerogen: A molecular simulation study. *J Nat Gas Sci Eng* 2016;31:738–46.
- [70] Liu L, Bhatia SK. Influence of morphology on transport properties and interfacial resistance in nanoporous carbons. *J Phys Chem C* 2019;123(34):21050–8. <http://dx.doi.org/10.1021/acs.jpcc.9b06270>, arXiv:https://doi.org/10.1021/acs.jpcc.9b06270.
- [71] Ho TA, Wang Y, Ilgen A, Criscenti LJ, Tenney CM. Supercritical CO_2 -induced atomistic lubrication for water flow in a rough hydrophilic nanochannel. *Nanoscale* 2018;10:19957–63. <http://dx.doi.org/10.1039/C8NR06204H>.
- [72] Zhang L, Li Q, Liu C, Liu Y, Cai S, Wang S, Cheng Q. Molecular insight of flow property for gas-water mixture ($\text{CO}_2/\text{CH}_4\text{-H}_2\text{O}$) in shale organic matrix. *Fuel* 2021;288:119720. <http://dx.doi.org/10.1016/j.fuel.2020.119720>, URL <https://www.sciencedirect.com/science/article/pii/S0016236120327162>.